Coastal Atmosphere & Sea Time Series (CoASTS) and Bio-Optical mapping of Marine optical Properties (BiOMaP): the CoASTS-BiOMaP dataset.

Giuseppe Zibordi[1] and Jean-François Berthon[2]

[1]*National Aeronautics and Space Administration, Goddard Space Flight Center, MD USA*
[2]*Joint Research Centre of the European Commission, Ispra, Italy*

Correspondence to: Giuseppe Zibordi (giuseppe.zibordi@eoscience.eu)

ABSTRACT

The *Coastal Atmosphere & Sea Time Series* (CoASTS) and the *Bio-Optical mapping of Marine optical Properties* (BiOMaP) programs produced bio-optical data supporting satellite ocean color applications for more than two decades. Specifically, relying on the Acqua Alta Oceanographic Tower (AAOT) in the northern Adriatic Sea, from 1995 till 2016 CoASTS delivered time series of marine water apparent and inherent optical properties, in addition to the concentration of major optically significant water constituents. Almost concurrently, from 2000 till 2022 BiOMaP produced equivalent spatially distributed measurements across major European Seas. Both, CoASTS and BiOMaP applied standardized instruments, measurement methods, quality control schemes and processing codes to ensure temporal and spatial consistency to data products. This work presents the CoASTS and BiOMaP near surface data products, named CoASTS-BiOMaP, of relevance for ocean color bio-optical modelling and validation activities.

1. Introduction

The validation of primary (*i.e.,* radiometric) and derived (*e.g.,* phytoplankton pigments concentration) satellite data products, as well as the development of bio-optical algorithms linking radiometric data to the inherent optical properties or to the concentration of natural water optically significant constituents, require accurate and comprehensive *in situ* bio-optical measurements (*e.g.,* see Werdell and Bailey 2007). Anticipating this need for the Sea-Wide Field-of-View (SeaWiFS) ocean color mission, during the 90s several measurement programs were established to gather bio-optical data representative of the world marine waters. Among these, the *Coastal Atmosphere & Sea Time Series* (CoASTS) and the *Bio-Optical mapping of Marine optical Properties* (BiOMaP) measurement programs implemented by the Marine Optical Laboratory (Belward et al. 2022) of the Joint Research Center (JRC) in collaboration with a number of European institutions, produced comprehensive *in situ* bio-optical measurements of relevance for satellite ocean color applications. While CoASTS benefited of the Acqua Alta Oceanographic Tower (AAOT) in the northern Adriatic Sea to generate time-series data at a fixed coastal site (Berthon et al. 2002; Zibordi et al. 2002), BiOMaP relied on oceanographic ships to collect spatially distributed measurements across various European Seas (Berthon et al. 2008, Zibordi et al. 2011). Both CoASTS and BiOMaP endorsed standardization of instruments, measurement methods, quality control schemes and processing codes to enforce consistency to temporally and spatially distributed data products. It is still recognized that some of the measurement methods primarily implemented for optically complex coastal waters, may not warrant the desirable high accuracy in oligotrophic clear waters.

Overall, CoASTS and BiOMaP data extend over a period exceeding two decades and constitute a unique dataset for bio-optical investigations across a variety of water types with potential application to climate change studies. Objective of this work is to introduce the CoASTS and BiOMaP derived data products relevant for satellite ocean color applications. Specifically, the near-surface data products with spectral values restricted to key ocean colour center-wavelengths are presented together with a description of the measurement and data reduction methods.

2. The CoASTS and BiOMaP programs

CoASTS and BiOMaP were conceived as complementary programs: CoASTS focused on the generation of time-series of reference data from a fixed coastal site showing significant seasonal cycles and moderate bio-optical complexity (Berthon et al. 2002); conversely BiOMaP covered a variety of marine regions exhibiting very diverse bio-optical regimes, but with limited temporal representativity (Berthon et al. 2008).

The use of an oceanographic tower as logistic platform for comprehensive optical and bio-geochemical measurements, when compared to oceanographic ships, does not allow for spatially extended observations. However, it offers the unique opportunity of a very stable measurement platform enabling easy control of the deployment geometry of optical instruments with respect to the structure. Specifically, regardless of sea state, the use of the AAOT as measurement platform made possible deploying optical sensors relying on tower–sensor–Sun geometry favouring the application of corrections for the minimization of potential superstructure perturbations in radiometric data (Zibordi et al. 1999, Doyle and Zibordi 2002).

CoASTS measurements are representative of marine frontal regions exhibiting occurrence of waters with optical properties largely determined by phytoplankton and its degradation components (*i.e.*, Case 1 waters), as wells as optically complex waters characterized

by moderate concentrations of sediments and coloured organic matter (CDOM), with bio-optical variability determined by the impact of local currents, seasonal changes in biological regimes and rivers discharge (Berthon et al. 2002).

CoASTS measurements took place with monthly occurrence since 1995. However, from 2001 and up to the end of the measurement program in 2016, the frequency of field measurements was reduced to one every 2-3 months. Each comprehensive data collection — called a *station* — included in-water optical and hydrographic profiles, seawater samples at different depths (*i.e.*, near surface, 8 m and 14 m), meteorological data, and visual observations of cloud cover and sea state. CoASTS comprises 176 field campaigns leading to 883 measurement stations. Still, only CoASTS campaigns and stations performed from December 1998 onward (*i.e.*, 125 and 617, respectively) fulfil the requirement of measurements standardization.

Spatially distributed measurements are best possible using oceanographic ships. Because of this, BiOMaP measurements were performed relying on research vessels across a variety of bio-optical regions (see Berthon et al. 2008): the Baltic Sea exhibiting waters dominated by a high concentration of CDOM; the Adriatic Sea, Black Sea, North Sea (including the English Channel), Ligurian Sea, Iberian Shelf and the Greenland Sea, characterized by a variety of optically complex waters determined by diverse concentrations of CDOM and suspended particulate matter (*SPM*); the Eastern and Western Mediterranean oligotrophic and mesotrophic Seas with optical properties largely determined by phytoplankton and its degradation components.

BiOMaP, encompassing 36 bio-optical oceanographic campaigns and 1915 measurement stations, started in 2000 and ended in 2022. It is mentioned that some measurements from 33 BiOMaP stations performed in the Black Sea during 2011 were included in an independent dataset constructed to support the validation of satellite data products (Valente et al. 2016).

As already anticipated, measurement consistency between the CoASTS and BiOMaP programs was achieved using identical field and laboratory instrumentation, and applying the same consolidated methods, quality control schemes and processing codes. Consequently, BiOMaP measurements performed during each station exhibit equivalence with those of CoASTS, except for restricting the collection of water samples to the near surface. Finally, superstructure perturbations in BioMaP radiometric data were avoided by operating optical radiometers on free-fall profilers deployed at some distance from ships (IOCCG 2019).

Figure 1 shows the temporal evolution of CoASTS measurement campaigns and the number of stations per campaign. These latter were largely benefitting of sea state conditions allowing access to the tower. Figure 2 shows the overall distribution of BiOMaP stations across the various European Seas.

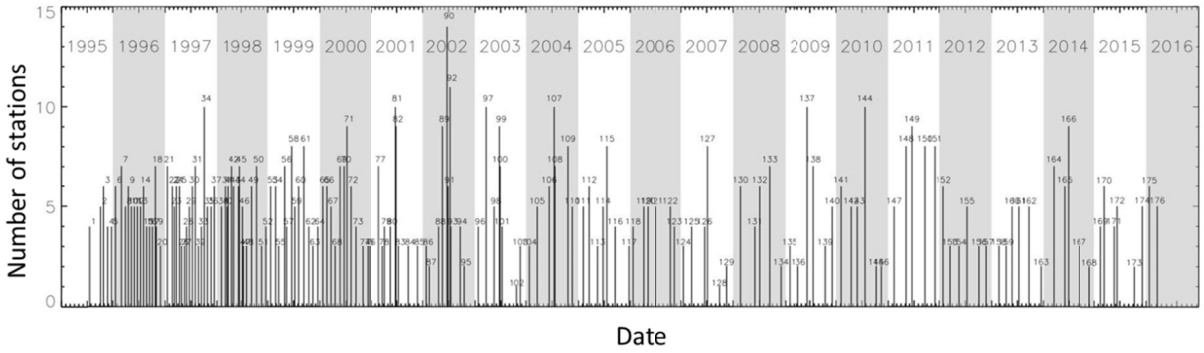

Figure 1. CoASTS measurement campaigns (176 total, 125 since December 1998) and stations (883 total, 637 since December 1998) completed between 1995 and 2016.

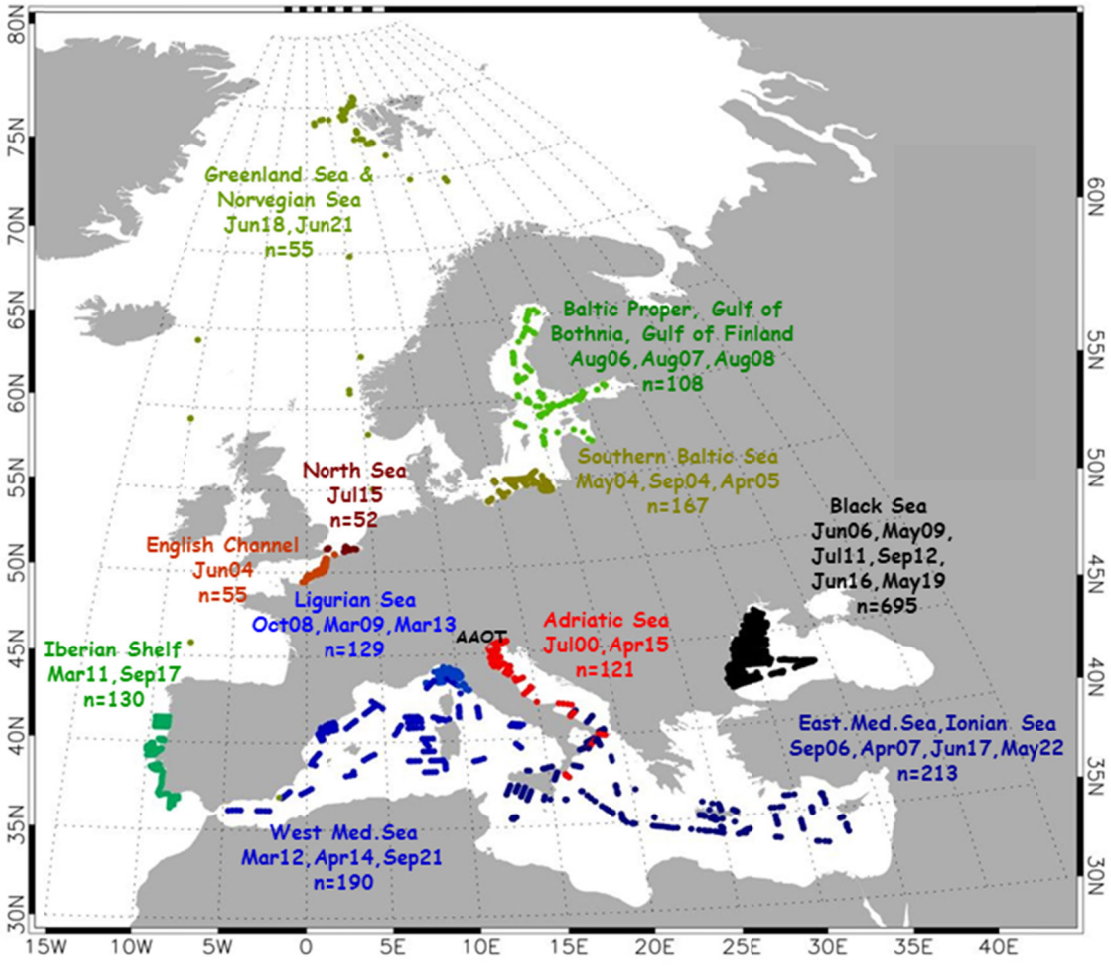

Figure 2. BiOMaP oceanographic campaigns (36) and measurement stations (1915) performed between 2000 and 2022.

Table 1. The CoASTS measurement program: campaign identifiers, marine region, years, number of stations, research platform, collaborating institution.

Campaign ID	Location	Year	Stations #	Research platform	Collaborating Institution
V03-V99	Northern Adriatic Sea (AAOT)	1998-2011	481	*Acqua Alta Oceanog. Tower (AAOT)*	Italian National Research Council (IT)
W01-W28	Northern Adriatic Sea (AAOT)	2011-2016	136	*Acqua Alta Oceanog. Tower (AAOT)*	Italian National Research Council (IT)

Table 2. The BiOMaP measurement program: campaign identifiers, marine regions, year, number of stations, research vessels, collaborating institutions.

Campaign ID	Region	Year	Stations #	Research vessel	Collaborating Institution
A01	Adriatic Sea (ADRS)	2000	55	*R/V Friuli-Venezia Giulia (FVG)*	University of Trieste (IT)
A02	Adriatic Sea (ADRS)	2014	66	*R/V Minerva-1*	Italian National Research Council (IT)
B01	Baltic Sea (BLTS)	2004	52	*R/V Oceania*	Institute of Oceanology (PL)
B02	Baltic Sea (BLTS)	2004	52	*R/V Oceania*	Institute of Oceanology (PL)
B03	Baltic Sea (BLTS)	2005	63	*R/V Oceania*	Institute of Oceanology (PL)
B04	Baltic Sea (BLTS)	2006	23	*R/V Aranda*	Institute of Marine Research (FI)
B05	Baltic Sea (BLTS)	2007	38	*R/V Aranda*	Institute of Marine Research (FI)
B06	Baltic Sea (BLTS)	2008	47	*R/V Aranda*	Institute of Marine Research (FI)
E01	Eastern Med. Sea (EMED)	2006	62	*R/V Urania*	Italian National Research Council (IT)
E02	Eastern Med. Sea (EMED)	2007	69	*R/V Urania*	Italian National Research Council (IT)
E03	Eastern Med. Sea (EMED)	2017	51	*R/V Minerva-1*	Italian National Research Council (IT)
E04	Eastern Med. Sea (EMED)	2022	31	*R/V Philia*	Hellenic Centre for Marine Research (GR)
I01	Iberian Shelf (IBSH)	2011	68	*NRP Almirante Gago Coutinho*	Portuguese Hydrographic Institute (PT)
I02	Iberian Shelf (IBSH)	2017	62	*NRP Almirante Gago Coutinho*	Portuguese Hydrographic Institute (PT)
K01	Black Sea (BLKS)	2006	93	*R/V Akademik*	Institute of Oceanology (BG)
K02	Black Sea (BLKS)	2009	73	*R/V Akademik*	Institute of Oceanology (BG)
K03	Black Sea (BLKS)	2009	40	*R/V Akademik*	Institute of Oceanology (BG)
K04	Black Sea (BLKS)	2011	38	*R/V Mare Nigrum*	National Institute of Marine Geology and Geoecology (RO)
K05	Black Sea (BLKS)	2011	24	*R/V Akademik*	Institute of Oceanology (BG)

K06	Black Sea (BLKS)	2011	59	*R/V Akademik*	Institute of Oceanology (BG)
K07	Black Sea (BLKS)	2012	93	*R/V Akademik*	Institute of Oceanology (BG)
K08	Black Sea (BLKS)	2012	14	*R/V Akademik*	Institute of Oceanology (BG)
K09	Black Sea (BLKS)	2016	54	*R/V Akademik*	Institute of Oceanology (BG)
K10	Black Sea (BLKS)	2016	83	*R/V Akademik*	Institute of Oceanology (BG)
K11	Black Sea (BLKS)	2019	80	*R/V Akademik*	Institute of Oceanology (BG)
K12	Black Sea (BLKS)	2019	44	*R/V Akademik*	Institute of Oceanology (BG)
L01	Ligurian Sea (LIGS)	2008	41	*R/V Alliance*	Undersea Research Center (NATO)
L02	Ligurian Sea (LIGS)	2009	63	*R/V Alliance*	Undersea Research Center (NATO)
L04	Ligurian Sea (LIGS)	2013	25	*R/V Alliance*	Undersea Research Center (NATO)
N01	English Channel & North Sea (NORS)	2004	55	*R/V Côtes de la Manche*	Université du Littoral Côte d'Opale (FR)
N02	North Sea (NORS)	2015	52	*R/V Belgica*	Royal Belgian Institute of Natural Sciences (BE)
O01	Western Med. Sea (WMED)	2012	73	*R/V Urania*	Italian National Research Council (IT)
O02	Western Med. Sea (WMED)	2014	64	*R/V Urania*	Italian National Research Council (IT)
O03	Western Med. Sea (WMED)	2021	53	*R/V Garcia del Cid*	Institute of Marine Science (ES)
P01	Greenland Sea (GRLS)	2018	15	*R/V Alliance*	Undersea Research Center (NATO)
P03	Greenland Sea[1] (GRLS)	2021	40	*R/V Alliance*	Italian Hydrographic Institute (IT)

[1] It includes stations from the Norwegian Sea.

3. Measurements overview

CoASTS and BiOMaP core data comprise *in situ* and laboratory measurements performed on samples prepared in the field. The firsts include:

a. Multispectral profiles of upwelling nadir radiance $L_u(z,\lambda)$, downward irradiance $E_d(z,\lambda)$, and upward irradiance $E_u(z,\lambda)$, were z indicates the depth and λ the center-wavelength of each spectral band;
b. Multispectral above-water downward irradiance $E_s(t,\lambda)$ acquired during in-water profiling (where t is the time corresponding to the depth z) and diffuse sky irradiance $E_i(t,\lambda)$ acquired at the end of each station with an irradiance sensor operated in conjunction with a rotating shadow band;
c. Multispectral profiles of beam attenuation $c(z,\lambda)$, absorption $a(z,\lambda)$ and backscattering $b_b(z,\lambda)$ coefficients, commonly restricted to the first 25 m depth for BiOMaP and 15 m for CoASTS;
d. Profiles of water temperature $T_w(z)$ and salinity $S_w(z)$, also restricted to the first 25 m depth for BiOMaP and 15 m for CoASTS;

e. Meteorological data including wind speed W_s in addition to cloud cover C_c and sea state S_s observations.

The laboratory measurements performed on field samples, complementary to the *in situ* ones, are:

f. Spectral *in vivo* particulate absorption coefficients $a_{ph}(\lambda)$ for the pigmented and $a_{dt}(\lambda)$ for the non-pigmented particles;
g. Spectral CDOM absorption coefficient $a_{ys}(\lambda)$;
h. Phytoplankton pigments concentration;
i. Suspended particulate matter concentration *SPM*.

4. Measurements and data reduction methods

Information on measurement methods and data reduction are summarized in the following subsections.

4.1 Radiometric products

CoASTS in-water radiometric measurements of $L_u(z,\lambda)$, $E_d(z,\lambda)$, $E_u(z,\lambda)$ were performed with the Wire-Stabilized Profiling Environmental Radiometer (WiSPER) using Satlantic (Halifax, Canada) OCR/OCI-200 multispectral radiometer series. Concurrently, above-water $E_s(t,\lambda)$ and $E_i(t,\lambda)$ measurements were also collected with OCI-200 radiometers. In the case of BiOMaP, the equivalent measurements were performed using miniPRO and microPRO Satlantic custom designed free-fall profilers equipped with OCR/OCI-200 or alternatively OCR-507 multispectral radiometers. All radiometric quantities were measured with 6 Hz acquisition rate at spectral bands relevant for ocean color applications with 10 nm bandwidth and nominal center-wavelengths at 412, 443, 490, 510, 555, 665 and 683 nm. WiSPER data were gathered with a deployment speed of 0.1 m s^{-1}. Conversely, the deployment speed of the free-fall systems generally varied in the range of approximately 0.3-0.4 m s^{-1}. The collection of in-water radiometric measurements with low tilt and as close as possible to the surface, was always attempted to ensure best retrieval of subsurface radiometric values through the extrapolation of profile data.

The regular absolute radiometric calibration of field optical radiometers was performed at the JRC Marine Optical Laboratory using 1000W FEL lamps traceable to the National Institute of Standards and Technology (NIST) or alternatively the National Physical Laboratory (NPL). While CoASTS radiometers were re-calibrated on a six-monthly basis, BiOMaP radiometers were calibrated before and after each oceanographic campaign. Regular inter-calibrations between the JRC Marine Optical Laboratory and the National Aeronautics and Space Administration (NASA) performed within the framework of the Ocean Color component of the Aerosol Robotic Network (AERONET-OC), ensured continuous verification of the accuracy of the calibration process (Zibordi et al. 2021).

Data pre-processing included: *i.* the application of absolute calibration coefficients and immersion factors for in-water radiometers (Zibordi et al. 2004; Zibordi 2006); *ii.* the removal of in-water and in-air data exhibiting tilt higher than 5° (this was confidently established from 2009 for BiOMaP $E_s(t,\lambda)$ and $E_i(t,\lambda)$); *iii*. limited to BiOMaP, the composition of successive profile data typically collected within a 5 min interval to create multi-cast combined profiles to increase the number of measurements per unit depth and consequently improve the precision of extrapolated values; and i*v.* the correction of in-air irradiance data for the non-cosine response of collectors (see Zibordi and Bulgarelli 2007). Additional corrections for sensors non-ideal

performance, such as out-of-band response or temperature dependence, were not implemented being considered minor for the multispectral instruments applied.

In agreement with consolidated protocols (*e.g.,* see IOCCG 2019), the impact of illumination changes in profile data were minimized through normalization of each radiometric quantity with respect to above–water downward irradiance $E_s(t,\lambda)$ simultaneous to the in-water measurements. Specifically, the normalization aimed at producing radiometric quantities as if they were taken at the same time t_0 at each depth z, where t_0 was chosen to coincide with the beginning of the acquisition sequence during each cast or multi-cast.

The sub-surface quantities $L_u(0^-,\lambda)$, $E_u(0^-,\lambda)$ and $E_d(0^-,\lambda)$ were then determined at the depth $z_0 = 0$ (identified by 0^-) as the exponentials of the intercepts resulting from the least-squares linear regressions of $\ln\Im(z,\lambda)$ versus z within the extrapolation interval z_0 - z_1, where $\Im(z,\lambda)$ indicates either $L_u(z,\lambda)$, $E_d(z,\lambda)$ or $E_u(z,\lambda)$ normalized with respect to $E_s(t,\lambda)$ at matching times. The extrapolation interval was chosen on a profile-by-profile basis with the aid of absorption and scattering profile data to identify the depths z_0 and z_1, generally comprised within 0.3 and 5 m and best satisfying the requirement of linear decay with depth of the log-transformed radiometric values. It is pointed out that the application of linear extrapolations to log-transformed data to determine sub-surface radiometric values, alternative to use of non-linear exponential extrapolations (see D'Alimonte et al 2012), was suggested by the objective to ensure consistency with existing radiometric data datasets.

Extreme outliers in the z_0 - z_1 depth interval generally due to major wave focusing and shadowing effects, were excluded from the extrapolation process by removing points exhibiting distance higher than $3\cdot\sigma$ from the linear regression line, where σ is the standard deviation of the differences between data points and regression line. This filtering process is mostly effective in the presence of a relatively small number of points in the extrapolation layer. The application of a very slow deployment speed in the case of CoASTS radiometric data and the application of the multi-cast method for BiOMaP data, ensured the availability of hundreds of measurements in each selected extrapolation interval. This restricts the application of the $3\cdot\sigma$ filter to a few extreme values without significantly impacting the precision of the extrapolated data.

The $L_u(0^-,\lambda)$ and $E_u(0^-,\lambda)$ data products were corrected for self-shading and potential bottom perturbations (Zibordi et al. 2002). Additionally, limited to CoASTS data collected in the vicinity of the AAOT, corrections were also applied for perturbations due to the deployment structure (Doyle and Zibordi 2002, Doyle et al. 2003). BiOMaP data, generally collected at distances from the ship of approximately 15–30 m, did not require corrections for the perturbations by the deployment structure.

In addition to $L_u(0^-,\lambda)$, $E_u(0^-,\lambda)$ and $E_d(0^-,\lambda)$, further retrieved data products are the slopes of the regression fits $K_\Im(\lambda)$ (*i.e.,* $K_L(\lambda)$, $K_u(\lambda)$ and $K_d(\lambda)$) in the extrapolation interval, *i.e.*, the diffuse attenuation coefficients. These $K_\Im(\lambda)$ values and particularly $K_d(\lambda)$, may exhibit underestimated values due to the impact of wave focussing in the near surface water layer. This effect is expected to be more pronounced for radiometric profiles collected in clear waters during clear sky conditions.

Derived radiometric data products are then the remote sensing reflectance $R_{rs}(\lambda)$

$$R_{rs}(\lambda) = L_w(\lambda)/E_s(\lambda) \quad (1)$$

and the normalized water–leaving radiance $L_{wn}(\lambda)$

$$L_{\mathrm{wn}}(\lambda) = R_{\mathrm{rs}}(\lambda) E_0(\lambda), \quad (2)$$

where $E_{\mathrm{s}}(\lambda)$ refers to the value measured at time t_0, $E_0(\lambda)$ is the extra-atmospheric solar irradiance (Thuillier et al. 2003) at the mean sun-earth distance, and $L_{\mathrm{w}}(\lambda)$ is the water–leaving radiance, *i.e.,* the radiance leaving the sea and quantified just above the surface through the extrapolation process, given by

$$L_{\mathrm{w}}(\lambda) = 0.544\, L_{\mathrm{u}}(0^{-}, \lambda). \quad (3)$$

where the factor 0.544 accounts for the radiance reduction across the water surface due to the change in the refractive index at the air–water interface, as determined assuming that the refractive index of seawater is independent of wavelength (Austin 1974). It is acknowledged that the values of $L_{\mathrm{w}}(\lambda)$ determined with Eq. 3 assuming a flat sea surface exhibit differences well within ±1% with respect to the values computed accounting for the spectral dependence of the water refractive index in the spectral range of interest (Voss and Flora 2017).

Finally, supplementary derived quantity is the Q-factor at nadir $Q_{\mathrm{n}}(0^{-},\lambda)$ determined by the ratio of $E_{\mathrm{u}}(0^{-}, \lambda)$ to $L_{\mathrm{u}}(0^{-}, \lambda)$ spectrally fitted to a quadratic function in the 412-555 nm spectral interval to minimize the impact of calibration and extrapolation uncertainties. The ratio of fitted $Q_{\mathrm{n}}(0^{-},\lambda)$ to $E_{\mathrm{u}}(0^{-}, \lambda)$ / $L_{\mathrm{u}}(0^{-}, \lambda)$ provides a basic approach to evaluate the relative consistency of the $E_{\mathrm{u}}(0^{-}, \lambda)$ and $L_{\mathrm{u}}(0^{-}, \lambda)$ multispectral values (*e.g.*, any appreciable bias affecting a single spectral value leads to a spectral inconsistency in $E_{\mathrm{u}}(0^{-}, \lambda)$ / $L_{\mathrm{u}}(0^{-}, \lambda)$).

The quantities $R_{\mathrm{rs}}(\lambda)$ and $L_{\mathrm{wn}}(\lambda)$, due to the normalization with respect to $E_s(\lambda)$, benefit of a first correction for changes in illumination conditions with sun zenith, sun-earth distance and atmospheric transmittance (Mueller and Austin 1995). The additional correction performed through the application of the $C_{f/Q}(\theta_0, \lambda, \tau_a, IOP)$ factors to $L_{\mathrm{wn}}(\lambda)$ and analogously to $R_{\mathrm{rs}}(\lambda)$, accounts for in-water bi-directional effects, and leads to the determination of the final $L_{\mathrm{WN}}(\lambda)$ and $R_{\mathrm{RS}}(\lambda)$ data products. The $C_{f/Q}$ factors are a function of the water inherent optical properties *IOP* (absorption and back-scattering coefficients), the atmospheric optical properties conveniently expressed through the aerosol optical depth τ_{a} and the sun zenith angle θ_0. These correction factors were determined applying the tabulated values proposed by Morel et al. (2002) for Case 1 waters with *IOPs* solely expressed as a function of total chlorophyll-*a* concentration (*Chla*) as determined from water samples for each measurement station. It is acknowledged that this correction may be affected by large uncertainties when applied to optically complex waters. Still, the inclusion of both $L_{\mathrm{w}}(\lambda)$ and $E_s(\lambda)$, as well as spectral values of the water inherent optical properties, would allow any potential user of the CoASTS-BiOMaP data set to implement alternative solutions for the determination of $L_{\mathrm{WN}}(\lambda)$ and $R_{\mathrm{RS}}(\lambda)$.

An estimate of the uncertainties for CoASTS and BiOMaP L_{WN} and similarly R_{RS} data, was attempted and discussed in various publications (Zibordi and Voss 2010, Zibordi et al. 2011) accounting for the major uncertainties characterizing: *i.* absolute calibration coefficients and immersion factors; *ii.* correction factors for shading perturbations; *iii.* correction factors for in-water bidirectional effects; *iv.* the determination of $E_{\mathrm{s}}(\lambda)$; *v.* the quantification of $E_0(\lambda)$ when ignoring actual bandwidths; *vi.* the extrapolation process for the computation of sub-surface data; and *vii.* finally, environmental stability as a result of wave perturbations and changes in illumination conditions and seawater optical properties during profiling. In the specific case of moderate optically complex waters such as those characterizing CoASTS measurements, the uncertainties affecting L_{WN} and R_{RS} are expected to approach 5% in the blue green spectral

region and 7% in the red. In agreement with analyses performed for alternative *in situ* radiometric methods (Gergely and Zibordi 2014), the above relative uncertainties may become significantly larger in the blue spectral region for data products from marine regions characterized by high water absorption such as the Baltic Sea.

Quality indices for radiometric products were determined during data processing in view of supporting an evaluation of their accuracy. These include: *i*. the ratio $Q_R(412) = Q_n(0^-,412) \ / \ Q_n(1,412)$ of Q_n values determined at 0^- and 1 m depths at the 412 nm center-wavelength, whose significant deviation from 1 suggests issues in the extrapolation of sub-surface values; *ii.* the coefficient of variation $CV\_E_s(412)$ of in-air downward irradiance for the extrapolation interval, whose high value indicates significant perturbations by ship movement or changes in illumination conditions during profiling; *iii.* the diffuse to direct ratio of above-water downward irradiance $R_d(412)$, whose high values indicates poor illumination conditions likely due to high sun zeniths or cloudiness; *iv.* the index $R_i(412) = E_s(412) \ / \ [1.04 \ E_d(412)]$, whose significant deviation from 1 indicates inconsistency between in-air and in-water measurements of the downward irradiance; and finally *v*. the index $K_i(490)$ determined by the difference between $K_d(490)$ and the corresponding value for pure water $K_w(490)$ set to 0.0212 m^{-1} (Smith and Baker 1981), whose negative value identifies radiometric data products (mostly related to clear waters and clear sky conditions) significantly challenged by wave perturbations.

4.2 Absorption and attenuation from profile data

Beam attenuation $c_{t\text{-}w}(z,\lambda)$ and absorption $a_{t\text{-}w}(z,\lambda)$ coefficients, excluding the contribution of pure seawater, were determined from measurements performed using AC9s instruments from WET Labs Inc. (Philomath, Oregon) with 25 cm path-length and nine spectral bands 10 mn wide at the 412, 440, 488, 510, 555, 630, 650, 676 and 715 nm center-wavelengths. The values of $c_{t\text{-}w}(z,\lambda)$ and $a_{t\text{-}w}(z,\lambda)$, in agreement with the scheme proposed by the instrument manufacturer (WET Labs 2006), were corrected for the effects of differences in temperature T_w and salinity S_w between field measurements and laboratory calibrations. These corrections were performed using $T_w(z)$ and $S_w(z)$ profile data simultaneous to the AC9 ones.

AC9 absorption coefficients need correction for the non-completely reflective surfaces of the absorption measurement tube, which prevents the collection of the whole scattered light and naturally leads to an overestimate of $a_{t\text{-}w}(z,\lambda)$. This correction was performed by removing a variable percentage of the scattering coefficient $b_{t\text{-}w}(z,\lambda)$ estimated from the difference between $c_{t\text{-}w}(z,\lambda)$ and $a_{t\text{-}w}(z,\lambda)$ at each λ, assuming the absorption coefficient of particulate and dissolved material is zero at the reference wavelength $\lambda_0 = 715$ nm and the shape of the volume scattering function is spectrally independent (Zaneveld et al. 1992). Recent investigations showed this correction method may lead to significant underestimates of $a_{t\text{-}w}(z,\lambda)$. Still, it was used in the CoASTS-BiOMaP data processing because alternative promising correction methods such as that proposed by Roettgers et al. (2013) may not be universally applicable (Stockley et al. 2017). Nevertheless, the potential for applying alternative scattering corrections is allowed by including in the dataset the absorption values at 715 nm, $a_{t\text{-}w}(z,715)$, not corrected for the scattering offset ($a_{t\text{-}w}(z,715)$ would be zero when corrected).

The additional correction for the finite acceptance angle of the detector, which would need additional field measurements of the volume scattering phase function (Boss et al. 2009) not included among the CoASTS and BiOMaP core data, could not be implemented.

In addition to regular instrument calibration and maintenance by the manufacturer, systematic AC9s pure water offsets were determined during each CoASTS campaign and at the

beginning and completion of each BiOMaP campaign in agreement with best practices for field operation. This offset accounts for any instrument response change while the AC9s are operated in their actual deployment configuration. The absorption and scattering offsets between the reference manufacturer calibrations and those performed in the field were applied as correction values. In the presence of appreciable offsets between successive field calibrations performed during the same campaign, differences were linearly interpolated over time.

Automated quality control was applied to each data record to verify the spectral and spatial (*i.e.,* vertical) consistency aiming at identifying those measurements affected by perturbations caused by bubbles or large particles flowing into the AC9 measurement chambers (*i.e.*, mostly individual spikes independently affecting $c_{t\text{-}w}(z,\lambda)$ or $a_{t\text{-}w}(z,\lambda)$ measurements especially in the surface layer). Specifically, $c_{t\text{-}w}(z,\lambda)$ and $a_{t\text{-}w}(z,\lambda)$ spectra exhibiting pronounced differences with respect to those characterizing the mean of profile spectra determined through a spectral consistency test, or pronounced changes with respect to depth at any λ identified through a spatial consistency test, were removed. The statistical parameters characterizing such a filtering process were tuned for profile data typical of individual campaigns in view of minimizing the potential for removing valid measurements.

The quality controlled $c_{t\text{-}w}(z,\lambda)$ and $a_{t\text{-}w}(z,\lambda)$ data were successively binned at 1 m resolution and retained when the depth d_b assigned to the center of the bin determined from the mean of the actual depths of individual measurements satisfies the condition $d_b = d_n \pm 0.25 \cdot d_i$, where d_n is the nominal depth of the center of the bin and d_i the bin width. The $c_{t\text{-}w}(\lambda)$ and $a_{t\text{-}w}(\lambda)$ values included in the CoASTS-BiOMaP dataset are the binned values tentatively corresponding to an average depth of 1 m.

A minimum uncertainty of 0.005 m^{-1} is assumed to affect AC9 measurements (Twardowski *et al.* 2001). Still, Stockley et al. (2017) showed that these values are largely underestimated especially in highly scattering waters in the blue-green spectral bands.

4.3 Backscattering from profile data

In situ vertical profiles of backscattering coefficients $b_b(z,\lambda)$ were determined using measurements performed with HydroScat-6 instruments from HOBI Labs Inc. (Tanque Verde, Arizona) in six bands 10 nm wide at the 442, 488, 510, 555, 620 and 676 (or 671) nm center-wavelengths. The values of $b_b(z,\lambda)$ were derived applying the conversion factor χ=1.08 to measurements of the volume scattering function $\beta(z,\psi,\lambda)$ performed at the sole scattering angle ψ=140° (Maffione and Dana 1997). The derived backscattering values were successively corrected for the water scattering and absorption applying the factor

$$\sigma_C(z,\lambda) = \exp\left[k_e(\lambda)\left(a(z,\lambda) + 0.4b(z,\lambda)\right)\right] \quad (4)$$

where $a(z,\lambda)$ and $b(z,\lambda)$ (with $b(z,\lambda)=c(z,\lambda)-a(z,\lambda)$) were obtained from AC9 measurements adding the pure water absorption and scattering coefficients, respectively, while the instrument specific spectral factors $k_e(\lambda)$ were those determined by the manufacturer during the initial calibration. Salinity corrections were applied considering *Fresh water* b_{bw} from Morel (1974) for the Black Sea and Baltic Sea measurements, and the *Salt water* b_{bw} from Morel (1974) for the other measurements. This solution, with respect to the use of actual salinity values may lead to misestimates of b_{bb} generally not exceeding 2% at 443 nm for the Baltic Sea and Black Sea.

The accuracy of the applied equation 4 was questioned by Doxaran et al. (2016). However, their newly derived relationship was determined from $b_b(550)$ values comprised in the 0-2.5 m^{-1} range while

the CoASTS and BiOMaP $b_b(555)$ values are lower than 0.1 m^{-1} with $a_{t\text{-}w}(555)$ not exceeding 1.0 m^{-1}. In this interval the equation proposed by Doxaran et al. (2016) does not appear to closely fit the plotted data (see their Fig. 5b). Because of this, still acknowledging their work, the processing equations originally proposed by Maffione and Dana (1997) for HydroScat-6 were applied

Equivalent to AC9 measurements, automated quality control was also applied to $b_b(z,\lambda)$ data to remove measurements exhibiting poor spectral and spatial (*i.e.,* vertical) consistency (*i.e.*, mostly individual spikes affecting $b_b(z,\lambda)$ at a single λ). By tuning the parameters defining the filtering process, spectra of $b_b(z,\lambda)$ exhibiting extreme differences with respect to the mean of profile spectra, or very high changes with depth at any λ, were removed. Quality controlled $b_b(z,\lambda)$ data were also binned at 1 m resolution adopting the same criteria applied for $a(z,\lambda)$ and $c(z,\lambda)$. The $b_b(\lambda)$ values included in the CoASTS-BiOMaP dataset are the binned values tentatively corresponding to an average depth of 1 m.

The quality index defined by the difference between $b_b(488)$ and the corresponding value $b_{bw}(488)$ is included in the dataset to identify those measurements mostly collected in very clear waters challenged by measurement uncertainties. The values of $b_{bw}(488)$, set equal to 0.001603 m^{-1} or alternatively equal to 0.001233 m^{-1} for the sole Black Sea and Baltic Sea data, were determined from those provided in Morel (1974) fitted according to Twardowski et al. (2007).

Annual factory calibrations performed at HOBILabs were complemented by pre-field laboratory verifications performed at the JRC Marine Optical Laboratory. These laboratory verifications aimed at correcting for HysdroScat-6 response changes between factory calibrations.

Whitmire et al. (2007) estimated minimum uncertainties of 0.0007 m^{-1} for measurements of $b_{bp}(z,\lambda)$ (*i.e.,* $b_b(z,\lambda)$ minus the backscattering of pure water) performed with HydroScat-6 instruments. Still, also in this case, actual uncertainties are expected to be much larger.

4.4 Absorption of particulate matter determined from discrete water samples

In vivo absorption coefficients $a_p(z,\lambda)$ of aquatic particles from water samples at discrete depths z were determined using the Transmission and Reflection (*T-R*) method proposed by Tassan and Ferrari (1995). This method was shown appropriate for any particle type, including highly back-scattering mineral particles or highly absorbing sediments. The method was implemented on a Perkin Elmer Lambda-19 and from 2004 on a Lambda-950, dual beam spectrometers equipped with integrating spheres.

Samples of particles were collected filtering water volumes on Whatman GF/F glass fibre filters with nominal pore size of 0.7 µm. Samples from the field were preserved in liquid nitrogen until laboratory analysis. The absorption coefficient $a_p(z,\lambda)$ of the equivalent particle suspension in the 400-750 nm spectral range with 1 nm resolution was determined from

$$a_p(z,\lambda) = 2.3\, A_s(z,\lambda)\, (F_a / V_w(z))^{-1} \quad (5)$$

where $V_w(z)$ is the volume of filtered water, F_a the filter clearance area and $A_s(z,\lambda)$ the equivalent particle suspension absorbance obtained with the *T-R* method.

The pigmented $a_{ph}(z,\lambda)$ and non-pigmented $a_{dp}(z,\lambda)$ fractions of the particulate absorption coefficient $a_p(z,\lambda)$ were obtained bleaching the sample using a solution of sodium hypochlorite (NaClO). The solution rapidly acts on pigment molecules and slowly on detritus making possible

418 a selective analysis of the two absorption components. A description of the bleaching technique
419 is presented in Tassan and Ferrari (1995) and in Ferrari and Tassan (1999).
420 Focused studies on the accuracy of the *T-R* method are given in Tassan and Ferrari
421 (1995) and in Tassan et al. (2000). Still, comprehensive uncertainty estimates for $a_{ph}(z,\lambda)$ and
422 $a_{dp}(z,\lambda)$ are not available. Nevertheless, dedicated analysis addressed the repeatability of in vivo
423 particulate absorption measurements performed with the *T-R* method (see Zibordi et al. 2002).
424 These investigated: *i*. repeated analysis of the same sample (*i.e.*, each sample was analysed
425 twice) and *ii*. the analysis of duplicate samples (*i.e.*, duplicates obtained from the same water
426 volume). Results for repeated analysis of the same samples showed mean absolute percent
427 differences of 2.9±2.3% at 443 nm with mean $a_p(443)$ = 0.082±0.042 m^{-1}, increasing up to
428 7.4±6.0% at 555 nm with mean $a_p(555)$ = 0.023±0.011 m^{-1}. These differences are attributed to: *i.*
429 method sensitivity, and *ii*. variations in the mechanical re-positioning of the sample in front of
430 the aperture of the integrating sphere combined with spatial non-homogeneities of the particles
431 distribution on the filter.
432 The analysis of duplicate samples showed mean absolute percentage differences of
433 8.9±5.9% at 443 nm with mean $a_p(443)$ = 0.090±0.049 m^{-1} and of 9.8±7.0% at 555 nm with
434 mean $a_p(555)$ = 0.024±0.012 m^{-1}. The former differences, increased by a few percent with
435 respect to those given for the repeated analysis of samples, are justified by: *i.* unavoidable
436 differences in replicates due to inhomogeneity affecting the particles distributions on filters; and
437 also *ii*. inhomogeneity in the distribution of particles in the water volumes used to produce the
438 samples. It is mentioned that an intrinsic error in the estimate of the actual particle absorption
439 coefficients results from the application of GF/F filters with nominal pore size of 0.7 µm. In fact
440 these filters do not allow bacteria and the fraction of mineral particles with diameter lower than
441 0.7 um to be accounted for. However, the absorption of these small mineral particles is generally
442 negligible compared to the total absorption, while the absorption of bacteria is almost 10 times
443 lower than that of algal cells and 5–10 times lower than that of cyanobacteria (Morel and Ahn
444 1990). The $a_{ph}(z,\lambda)$ and $a_{dp}(z,\lambda)$ measurements included in the CoASTS-BiOMaP dataset refer to
445 water samples collected at approximately 1 m depth.
446
447 ***4.5 Absorption of CDOM determined from discrete water samples***
448 The absorption coefficient $a_{ys}(z,\lambda)$ of CDOM at depth z was determined applying the
449 method detailed in Ferrari et al. (1996) using a Perkin Elmer Lambda-12 and from 2010 a
450 Lambda-35 dual-beam spectrometers. Samples were prepared by filtering water volumes on
451 Millipore 0.22 µm pore size cellulose filters and adding a solution of 10 gl^{-1} of NaN_3 to the
452 filtered water to prevent bacteria growth (typically 1 ml of the solution was added to 100 ml of
453 filtered water).
454 CDOM samples were preserved at approximately 4^0C in an amber glass bottle until
455 laboratory analysis. The spectrometric measurements, generally carried out within a few days
456 from the completion of the measurement campaign, were performed with 1 nm resolution in the
457 350-750 nm spectral region. Measurements were performed placing a 10 cm quartz cuvette
458 containing pure milli-Q water in the optical path of the reference beam, and a 10 cm quartz
459 cuvette containing the CDOM sample in the optical path of the sample beam. It is acknowledged
460 that the 10 cm path-length systematically applied for the analysis of CoASTS and BiOMaP field
461 samples, naturally challenges the accuracy of measurements characterized by low CDOM
462 absorption such as those from the Eastern Mediterranean Sea.

The spectral absorption coefficient $a_{ys}(z,\lambda)$ was computed from the measured absorbance $A_{ys}(z,\lambda)$ resulting from the difference between the sample absorbance and the reference absorbance (Ferrari et al., 1996), as

$$a_{ys}(z,\lambda) = 2.3\, A_{ys}(z,\lambda)\, L_c^{-1} \quad (6)$$

where L_c is the pathlength of the cuvette.

Assuming CDOM does not absorb in the red and following community recommendations (see Section III in IOOCG 2019), the absorption coefficients are corrected for the background offset by subtracting to $a_{ys}(z,\lambda)$ the mean of $a_{ys}(z,\lambda_i)$ spectral values for λ_i in the 670-680 nm interval.

Comprehensive uncertainty values are also not available for $a_{ys}(z,\lambda)$. Still, the repeatability of $a_{ys}(z,\lambda)$ measurements (see Zibordi et al. 2002) was also investigated through: *i.* repeated analysis of the same samples; and *ii.* the analysis of duplicate samples. The repeated analysis of the same samples showed average absolute percent differences varying as a function of the absorption value from 10.1±7.3% at 412 nm with mean $a_{ys}(z,412)$ = 0.168±0.037 m^{-1} up to 24.2±19.8% at 555 nm with mean $a_{ys}(z,555)$ = 0.015±0.005 m^{-1}. These differences are mostly ascribed to the precision of the method. The analysis of the duplicate samples showed expected augmented average absolute percent differences when compared to repeated analysis of samples varying from 12.1±6.3% at 412 nm with mean $a_{ys}(z,412)$ = 0.175±0.038 m^{-1} and up to 30.3±23.8% at 555 nm with mean $a_{ys}(z,555)$ = 0.018±0.005 m^{-1}. The latter increased values are largely justified by differences between samples.

It is finally mentioned that the use of 0.22 µm pore size filters to produce CDOM samples, when the 0.7 µm pore size filters are applied for the quantification of particle absorption coefficients, suggests that the overall absorption budget cannot be fully resolved. In fact, as already anticipated, bacteria and very small mineral particles having size between 0.2 and 0.7 µm, are not included in the absorption analysis. Still, this missing contribution to the overall absorption budget is expected to be minor.

As per $a_{ph}(\lambda)$ and $a_{dp}(\lambda)$, also the $a_{ys}(\lambda)$ measurements included in the CoASTS-BiOMaP dataset refer to water samples collected at approximately 1 m depth.

4.6 Pigments concentration

Phytoplankton pigment concentrations were determined by using High Performance Liquid Chromatography (HPLC) with the method proposed by Van Heukelem and Thomas (2005). Exceptions are the samples collected before 2000 for which the method proposed by Jeffrey et al. (1997) was applied.

The analysis were performed on samples of particulate matter retained on GF/F filters with a nominal pore size of 0.7µm: this choice is justified by the diameter of living phytoplankton cells generally higher than 1 µm (Stramsky and Kiefer, 1991). After filtration, samples were preserved in liquid nitrogen until laboratory analysis.

Following Van Heukelem and Thomas (2005), the samples were transferred to vials with 3 ml 95% acetone and vitamin E as internal standard. Samples were then disrupted using a vortex mixer, sonicated on ice, extracted at 4°C for 20 h, and mixed again. The samples were successively filtered through 0.2 µm Teflon syringe filter into HPLC vials and placed in the cooling rack of the HPLC system. Buffer and sample were injected in the HPLC (Shimadzu LC-

10A or alternatively an HP-1100, systems) in the 5/2 ratio using a pre-treatment program and mixing in the loop before injection.

The list of pigments systematically analysed at the JRC Marine Optical Laboratory or alternatively at DHI A/S (Hørsholm, Denmark) includes: chlorophyll a (resulting from the sum of divinyl- and monovinyl-chlorophyll a), chlorophyll b, chlorophyll c_1+c_2, chlorophyllide a, fucoxanthin, diadinoxanthin, β-carotene, zeaxanthin, alloxanthin, 19'-butanoyloxyfucoxanthin, 19'-hexanoyloxyfucoxanthin and diatoxanthin.

Various inter-comparisons of HPLC methods performed within the framework SeaWiFS HPLC Analysis Round-Robin Experiments (SeaHARRE) organized by NASA with the JRC participation, demonstrated the capability of various laboratories to achieve differences lower than 6% in the determination of total chlorophyll *a* concentration *Chla* (*i.e.*, the sum of chlorophyll *a* and chlorophyllide *a*) and lower than 25% for the other ancillary pigments characterizing marine waters (Hooker et al. 2010). The analysis of CoASTS and BiOMaP shows *Chla* values always higher than 0.03 - 0.04 $\mu g\ l^{-1}$. This may suggest some quantification limit for the methodology applied to determine pigments concentration.

Consistent with $a_{ph}(z,\lambda)$, $a_{dp}(z,\lambda)$ and $a_{ys}(z,\lambda)$, measurements of *Chla* were performed on water samples collected at approximately 1 m depth.

4.7 Suspended particulate concentration

The concentration of suspended particulate matter, *SPM,* was obtained from the net weight of the particulate material collected on filters following the method detailed in Van der Linde (1998) as an evolution of that proposed by Strickland and Parsons (1972). Samples were produced by filtering volumes of water on GF/F filters with 0.7 μm nominal pore size previously baked at 450 ^{0}C for 1 hour, pre-washed, dried for 1 hour at 75 ^{0}C and finally pre-weighted on a electrobalance. After water filtration, the filters (*i.e.*, filtration area and border) were washed with distilled water and stored at –18 ^{0}C for successive laboratory analysis. Before final weighting, the filters were dried at 75 ^{0}C for 1 hour, and then temporarily stored in a desiccator.

The concentration of *SPM* was calculated from

$$SPM\,(z) = [(W_f(z) - W_s(z)\,) - w_b]V(z)^{-1} \qquad (7)$$

where $W_f(z)$ is the weight of the filter before filtration, $W_s(z)$ is the weight of the filter after filtration, $V(z)$ is the volume of the filtered water and w_b is a correction term introduced to account for variations in the weight of the filter sample due to changes in environmental conditions between the two weightings steps. The values of w_b were determined from *blank* filters (*i.e.,* GF/F filters completely conditioned, not used for water filtration, but exposed to the same processes of the sample filters: transportation to the measurement site and back, storage in the freezer, drying). The w_b values applied in Eq. 7, are the differences between the average final weight of *blank* filters and their original average weight.

SPM values included in the CoASTS-BiOMaP data set are generally obtained from the average of duplicate samples. In the case of large differences between duplicates (*i.e.*, tentatively exceeding 20%) the *SPM* value from one of the two samples is used prior investigating the surface and integrity of the samples, and also verifying the consistency of their values with AC9 measurements from close stations.

The use of GF/F filters with 0.7 μm nominal pore size for *SPM* analysis leads to an underestimate of total suspended matter due to the loss of particles with diameter lower that 0.7

554 µm. However, it is recognized that the filter rinsing for salt removal and the filter conditioning
555 after filtration before final weighting, can induce errors certainly much larger than the mass of
556 particles with diameter lower than 0.7 µm.
557 An analysis of measurement repeatability performed with duplicate samples showed mean
558 percent difference equal to 13.9±13.4% with mean $SPM(z)$ = 0.86±0.40 mg·l^{-1}. The largest
559 differences between duplicate samples (*i.e.,* larger than 30%) were observed with values of
560 $SPM(z)$ lower than approximately 0.5 mg l^{-1}. This is explained by the intrinsic uncertainty
561 affecting sample preparation (*i.e.,* water sample non-homogeneity and filter rinsing).
562 As for other quantities determined from the analysis of water samples, also the *SPM* values
563 included in the CoASTS-BiOMaP dataset refer to samples collected at approximately 1 m depth.
564
565 ***4.8 Salinity and temperature***
566 Profiles of salinity $S_w(z)$ and temperature $T_w(z)$ measurement were performed with SBE
567 19-plus Conductivity-Temperature-Depth (CTD) sensors from Sea-Bird Scientific (Bellevue,
568 Washington). These devices were calibrated by the manufacturer approximately on a two-year
569 basis. Uncertainties are tentatively expected to be within 0.01‰ for salinity and 0.01ºC for
570 temperature.
571 Equivalent to $a(z,\lambda)$, $c(z,\lambda)$ and $b_b(z,\lambda)$ profiles, automated quality control was also
572 applied to $S_w(z)$ and $T_w(z)$ data to remove measurement artefacts. By trimming filtering parameters
573 to individual campaigns, values of $S_w(z)$ and $T_w(z)$ exhibiting extreme changes with respect to
574 depth, were removed. Quality checked $S_w(z)$ and $T_w(z)$ data were binned at 1 m resolution
575 adopting the same criteria already applied for $a(z,\lambda)$, $c(z,\lambda)$ and $b_b(z,\lambda)$. The values associated
576 with the first bin, tentatively representing the 1 m depth, are included in the CoASTS-BiOMaP
577 dataset.
578
579 ***4.9 Meteorological and environmental observations***
580 Among the meteorological quantities and observations recorded during each measurement
581 station, the wind speed W_s, sea state S_s and cloud cover C_c are included in the data set.
582
583 **5. The near-surface CoASTS and BiOMaP dataset (CoASTS-BiOMaP)**
584 CoASTS-BiOMaP data are accessible at https://doi.org/10.1594/PANGAEA.971945 in
585 tabular form and include the near-surface data products from CoASTS and BiOMaP
586 measurements of relevance for the validation of satellite ocean color data and the development of
587 bio-optical algorithms. All spectral data products are restricted to the nominal center-
588 wavelengths 412, 443, 490, 510, 555, 665 nm, unless diversely specified. CoASTS data products
589 are only provided from December 1998 when full standardization of measurements and
590 processing was put in place. In addition, station data were excluded from CoASTS-BiOMaP
591 when the $L_{WN}(\lambda)$ or $K_d(\lambda)$ radiometric products did not satisfy basic quality control criteria by
592 exhibiting spectra with unexplained shape or amplitude. Furthermore, poor quality of data
593 products other than radiometric, implied the exclusion of their individual values from the dataset.
594 Table 3 provides a comprehensive list of the quantities included in the CoASTS-BiOMaP
595 dataset: each one is identified by a convenient symbol, a brief description and its physical units.
596 A summary of the average values of the major bio-optical and hydrographic quantities
597 determined for the various marine regions is provided in Table 4. These are: the diffuse
598 attenuation coefficient K_d at 490 nm, the water absorption coefficient (from discrete sample

599 analysis, pure water contribution excluded) a at 490 nm, the backscattering coefficient (water
600 contribution included) b_b at 488 nm; the concentrations of total chlorophyll-a *Chla* and
601 suspended particulate matter *SPM*; and the salinity S_w. All quantities exhibit ample differences
602 across the various marine regions. Notable, variations in $K_d(490)$ exceed one order of magnitude
603 between the Eastern Mediterranean (EMED) and the Baltic Sea (BLTS) waters (*i.e.,* $K_d(490)$
604 varies from 0.037 to 0.494 m^{-1}).
605 Figure 3 displays BioMaP and CoASTS $L_{WN}(\lambda)$ spectra for the different marine regions.
606 These spectra clearly indicate diverse bio-optical features for the different regions. They span
607 from the highly oligotrophic Eastern Mediterranean Sea (EMED) showing maximum values in
608 the blue region, to the optically complex Baltic Sea (BLTS) dominated by the presence of high
609 concentrations of CDOM as expressed by low values of L_{WN} in the blue spectral region. Between
610 these, there are marine regions exhibiting diverse bio-optical complexity due to different
611 concentration of optically significant constituents. Notably, some spectra from the North Sea
612 (NORS) indicate the presence of relatively high concentration of sediments, while spectra from
613 the Black Sea (BLK) and the northern Adriatic Sea (AAOT) suggest bio-optical conditions
614 determined by the presence of various concentrations of SPM and CDOM determining L_{WN}
615 maxima at the 510 or 555 nm center-wavelengths.
616 Table 5 provides the mean spectral values and related standard deviations of $Q_n(\lambda)$ for the
617 various marine regions as determined from radiometric profiles performed during near clear sky
618 conditions determined by $Cc \leq 1/4$. These naturally exhibit some spectral dependence varying
619 with the water type. For instance, $Q_n(\lambda)$ from the Eastern Mediterranean Sea (EMED) exhibit
620 almost spectrally constant mean values approaching 4 sr in the 412-555 nm spectral interval and
621 of approximately 5 sr at 665 nm. Conversely, regions such as the northern Adriatic Sea (AAOT)
622 exhibit mean values approaching 4.5 sr with some spectral dependence in the 412-555 nm
623 spectral region, and also a mean value of 5 sr at 665 nm.
624 Figure 4 displays the $a_{ph}(\lambda)$ spectra for the CoASTS and BioMaP regions. Notable is the
625 increase in the values of mean $a_{ph}(443)$ from 0.007 m^{-1} for the Eastern Mediterranean Sea
626 (EMED) to 0.191 m^{-1} and 0.220 m^{-1} for the Baltic Sea (BLTS) and North Sea (NORS),
627 respectively. The peculiar spectra shown by North Sea stations off the Belgian coast exhibiting
628 a_{ph} values higher at 412 nm than at 443 nm (see panel for NORS data in Fig. 4), are explained by
629 high concentrations of pheophytin leading to an increase of the absorption coefficient toward 412
630 nm.
631 Figure 5 displays the comparison of the near surface absorption coefficients (pure water
632 excluded) determined from AC9 measurements at the center-wavelength of 443 nm, $a_{t\text{-}w}$(AC9),
633 versus the equivalent absorption coefficients determined from water samples, $a_{t\text{-}w}$(sample)=
634 $a_{ph}(443)+a_{dt}(443)+a_{ys}(443)$. Results suggest an increasing underestimate of $a_{t\text{-}w}$(AC9) and larger
635 relative scattering with a decrease in absorption. This is highlighted by the scatter plots of data
636 from the Eastern Mediterranean Sea (EMED) exhibiting an underestimate exceeding 70% with
637 values of $a_{t\text{-}w}$(samples) generally lower than 0.1 m^{-1}. Conversely, the Baltic Sea (BLTS) shows
638 outstanding agreement between the compared quantities with absorption values comprised in the
639 range of 0.2-1.2 m^{-1}. These mean differences between $a_{t\text{-}w}$(AC9) and $a_{t\text{-}w}$(samples) absorption
640 values could be explained by an incomplete correction of the perturbing effects due to finite
641 acceptance angle of the detector, the non-fully reflective surface of the AC9 absorption chamber
642 (*i.e.*, the two short 25 cm path-length tubes) and also by the non-negligible absorption of
643 particles at the reference wavelength $\lambda_0 = 715$ nm applied for scattering corrections.
644

645 Table 3. The CoASTS-BiOMaP data set: quantities identified by symbols, description of
646 quantities and related units.

Symbol	***Description***	***Units***	***Details***
Station_ID	Station identifier	Code	*Gccssii*[(1)]
Date&Time	Date and time	GMT	*yyyy-mm-dd*T*hh:mm:ss*[(2)]
Lon	Longitude	Degrees	
Lat	Latitude	Degrees	
Sz	Sun zenith	Degrees	
Sa	Sun azimuth	Degrees	
$L_u(\lambda)$	Upwelling radiance at depth 0^-	W m^{-2} nm^{-1} sr^{-1}	At nominal λs[(3)]
$E_d(\lambda)$	Downward irradiance at depth 0^-	W m^{-2} nm^{-1}	At nominal λs[(3)]
$E_u(\lambda)$	Upward irradiance at depth 0^-	W m^{-2} nm^{-1}	At nominal λs[(3)]
$K_L(\lambda)$	Diffuse att. coeff. from $L_u(z,\lambda)$	m^{-1}	At nominal λs[(3)]
$K_d(\lambda)$	Diffuse att. coeff. from $E_d(z,\lambda)$	m^{-1}	At nominal λs[(3)]
$K_u(\lambda)$	Diffuse att. coeff. from $E_u(z,\lambda)$	m^{-1}	At nominal λs[(3)]
$E_s(\lambda)$	Downward irradiance at depth 0^+	W m^{-2} nm^{-1}	At nominal λs[(3)]
$Q_n(\lambda)$	Q-factor an nadir at depth 0^-	sr	At nominal λs[(3)]
$R_{RS}(\lambda)$	Remote sensing reflectance at depth 0^+	sr^{-1}	At nominal λs[(3)]
$L_{WN}(\lambda)$	Normalized water-leaving rad. at depth 0^+	W m^{-2} nm^{-1} sr^{-1}	At nominal λs[(3)]
$Q_R(412)$	Ratio of $Q_n(412)$ at depth 0- to $Q_n(1,412)$ at 1 m depth	–	Introduced to best support the use of $Q_n(\lambda)$ (large deviations from 1 may indicate extrapolation issues)
$R_d(412)$	Ratio of the diffuse $E_i(412)$ to direct $[E_s(412) - E_i(412)]$ above-water downward irradiance at 412 nm	–	
*CV_*$E_s(412)$	Coefficient of variation E_s (412)	%	
$R_i(412)$	Ratio of the above-water downward irradiance $Es(412)$ to the in-water downward irradiance $E_d(412)$ multiplied by 1.04	–	
$K_i(490)$	Diffuse attenuation coefficient $K_d(490)$ minus the diffuse attenuation coefficient of pure sea water $K_w(490)$ assumed constant and equal to 0.0212	m^{-1}	Introduced to best support the exploitation of data (a negative value may suggest extrapolation challenged by wave perturbations)
$a_{ph}(\lambda)$	Absorption coefficient by pigmented particles at 1 m depth	m^{-1}	At nominal λs[(3)]
$a_{dt}(\lambda)$	Absorption coefficient by non-pigmented part. at 1 m depth	m^{-1}	At nominal λs[(3)]
$a_{ys}(\lambda)$	Absorption coefficient by CDOM at 1 m depth	m^{-1}	At nominal λs[(3)]
$a_{t\text{-}w}(\lambda)$	Absorption coefficient from AC9 at 1 m depth	m^{-1}	At AC9 λs[(4)]. The values $a_{t\text{-}w}(715)$ are not corrected for the scattering offset. If corrected, their values would be zero.
$c_{t\text{-}w}(\lambda)$	Beam attenuation coefficient from AC9 at 1 m depth	m^{-1}	At AC9 λs[(4)]
$b_b(\lambda)$	Backscattering coefficient from HydroScat-6 at 1 m depth	m^{-1}	At HydroScat-6 λs[(5)]
$b_b(488)$ - $b_{bw}(488)$	Backscattering coefficient $b_b(488)$ minus	m^{-1}	Introduced to best support the

	the backscattering coefficient of pure sea water $b_{bw}(488)$ assumed constant and equal to 0.001603 m^{-1} or alternatively 0.001233 m^{-1} for the sole Black Sea and Baltic Sea measurements		exploitation of data (a negative value may indicate measurements challenged by significant uncertainties)
Chla	Total chlorophyll-*a* concentration at 1 m depth [6]	µg l^{-1}	
SPM	Suspended particulate matter concentration at 1 m depth	mg l^{-1}	
T_w	Temperature of seawater at 1 m depth	°C	
S_w	Salinity of seawater at 1 m depth	‰	
W_s	Wind speed	m s^{-1}	
S_s	Sea state	0-9	WMO scale
C_c	Cloud cover	0-4	Octa/2

[1] *G* indicates the site or geographic region (*V* and *W* for AAOT, *A* for Adriatic Sea, *B* for Baltic Sea, *E* for Eastern Mediterranean Sea, *K* for Black Sea, *L* for Ligurian Sea, *N* for North Sea, *O* for Western Mediterranean Sea, *I* for Iberian Shelf, *P* for Greenland Sea), while *cc* indicates the campaign number for the specific region, *ss* the station number and *ii* the cast number.

[2] The letters *yyyy* indicate the year, *mm* the month, *dd* the day *hh,* the hours and *mm* the minutes.

[3] Nominal center-wavelengths for radiometric data products are 412, 443, 490, 510, 555 are 665 nm.

[4] Center-wavelengths for AC9 data products are 412, 440, 488, 510, 555, 630, 650, 676, and 715 nm.

[5] Center-wavelengths for HydroScat-6 data products are 442, 488, 510, 555, 620, and 676 (or 671) nm.

[6] Total chlorophyll-*a* concentration indicates the sum of chlorophyllide-*a*, monovinyl- and divinyl-chlorophyll-*a*.

Table 4. Mean ± standard deviations of quantities describing the bio-optical and hydrographic characteristics of the CoASTS and BioMaP marine regions: the diffuse attenuation coefficient K_d at 490 nm; the seawater absorption coefficient (excluding pure water contribution) *a* determined from discrete sample analysis at 490 nm; the backscattering coefficient (including pure water contribution) b_b at 488 nm; the concentrations of total chlorophyll-a *Chla* and suspended particulate matter *SPM*; and finally the salinity *Sw*.

Region	$K_d(490)$[m^{-1}]	$a(490)$ [m^{-1}]	$b_b(488)$[m^{-1}]	*Chla*[µg l^{-1}]	*SPM*[mg l^{-1}]	S_w[‰]
EMED	0.037±0.022	0.031±0.012	0.0026±0.0007	0.09±0.08	0.27±0.45	38.6±0.7
WMED	0.046±0.025	0.040±0.019	0.0032±0.0009	0.30±0.37	0.30±0.22	37.8±0.4
IBSH	0.084±0.049	0.073±0.033	0.0040±0.0023	0.81±0.83	0.53±0.39	36.0±0.2
GRLS	0.097±0.062	0.082±0.032	0.0039±0.0021	0.94±1.04	0.64±0.28	34.0±1.6
LIGS	0.110±0.079	0.079±0.045	0.0078±0.0067	0.93±0.85	0.71±0.57	37.7±1.0
ADRS	0.141±0.125	0.085±0.059	0.0090±0.0067	1.25±1.32	1.14±1.45	35.6±2.3
AAOT	0.176±0.102	0.099±0.053	0.0121±0.0073	1.28±1.13	1.25±0.76	34.9±2.3
BLKS	0.219±0.254	0.131±0.130	0.0093±0.0066	1.62±3.13	1.17±1.24	16.6±1.8
NORS	0.876±0.864	0.377±0.346	0.0197±0.0160	4.23±2.27	9.96±12.52	33.7±1.4
BLTS	0.494±0.409	0.308±0.269	0.0107±0.0084	4.99±8.04	1.53±1.71	6.2±1.4

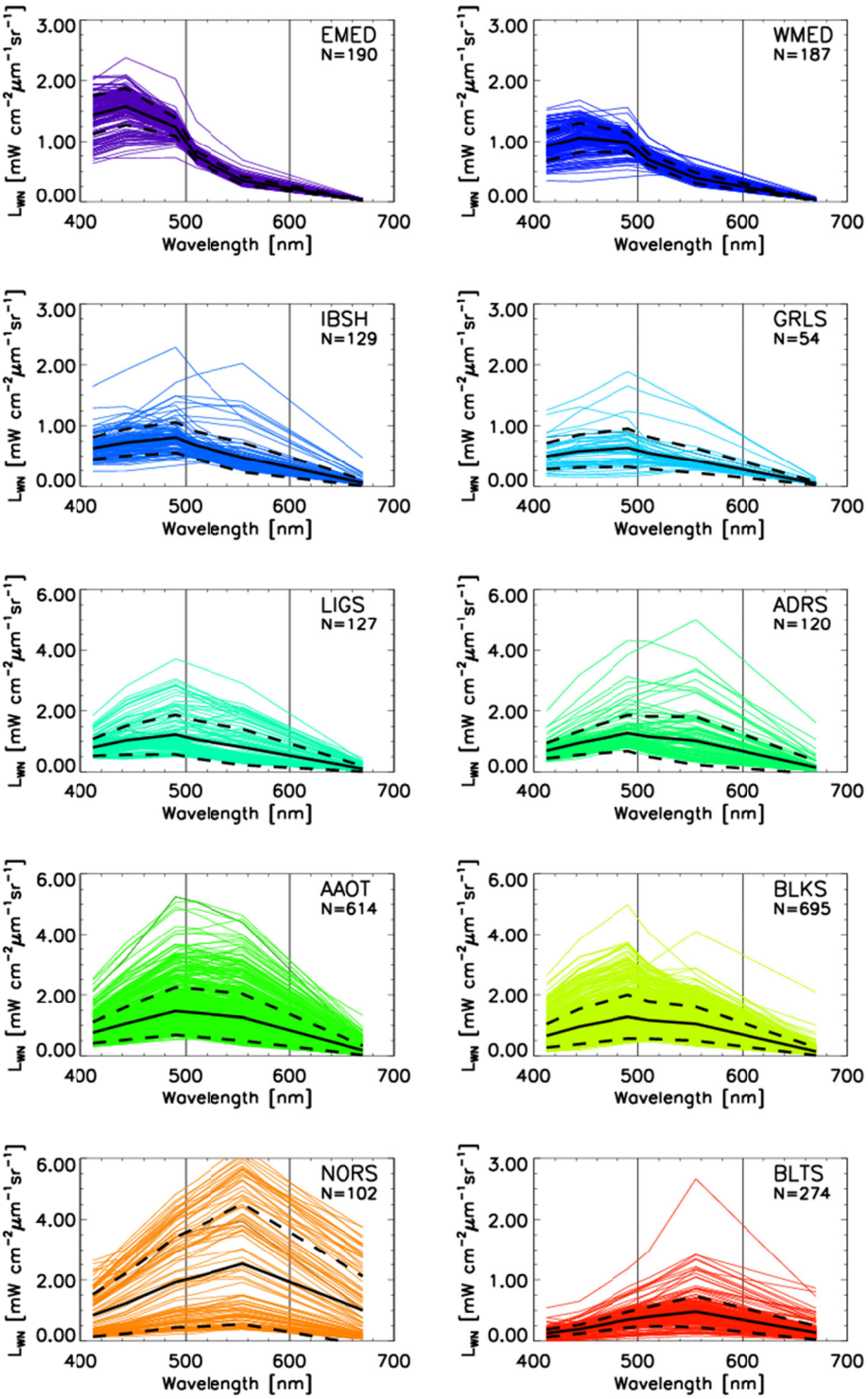

Figure 3. Spectra of $L_{WN}(\lambda)$ for the CoASTS and BioMaP geographic regions (see Table 1 for acronyms). N indicates the number of spectra. The continuous black lines indicate mean values while the dashed lines indicate ± 1 standard deviation. For convenience, the spectra are plotted in units of mW cm^{-2} μm^{-1} sr^{-1}.

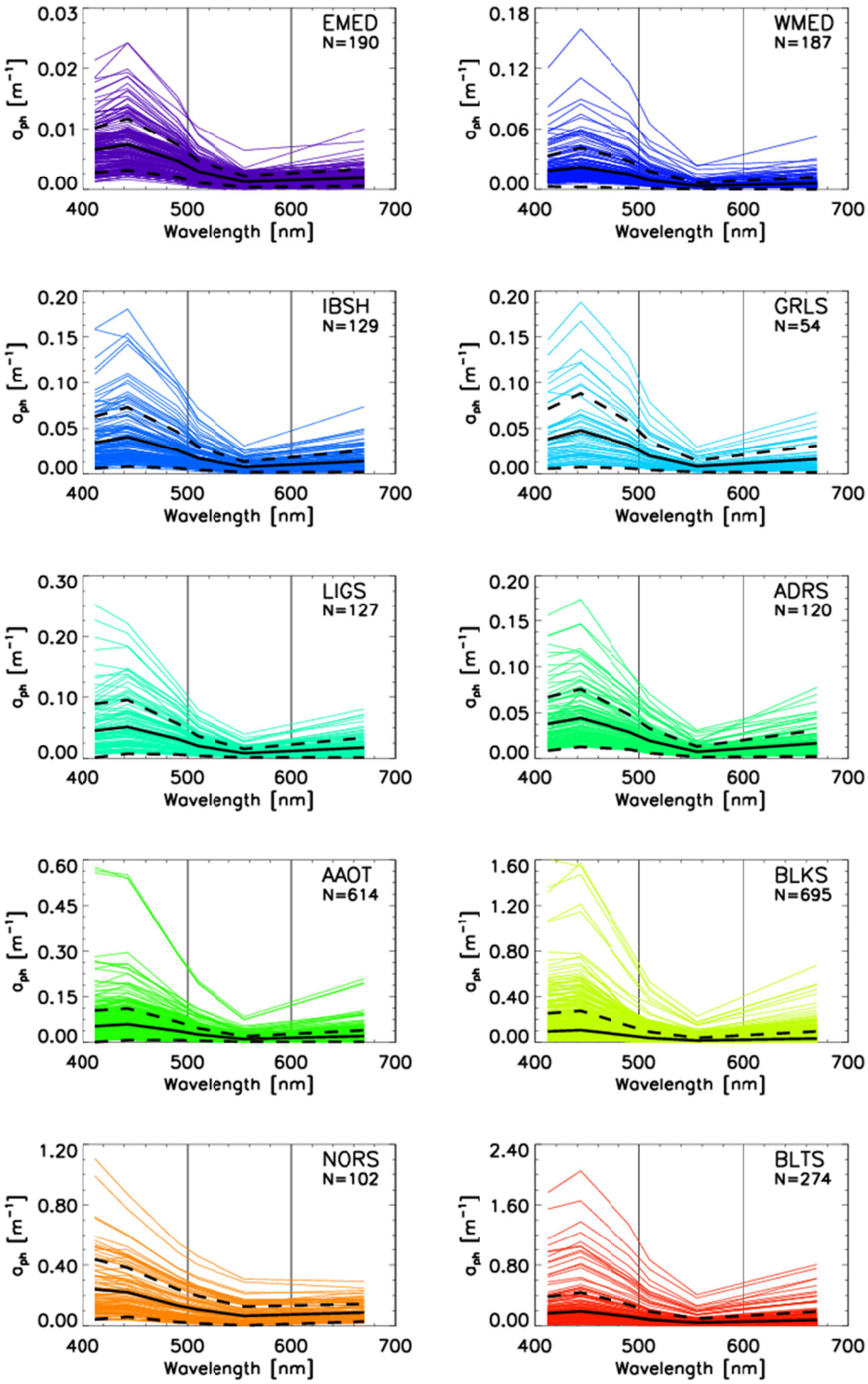

672

673 Figure 4. Spectra of $a_{ph}(\lambda)$ for the CoASTS and BioMaP marine regions. N indicates the number
674 of spectra. The continuous black lines indicate mean values while the dashed lines indicate ± 1
675 standard deviation.

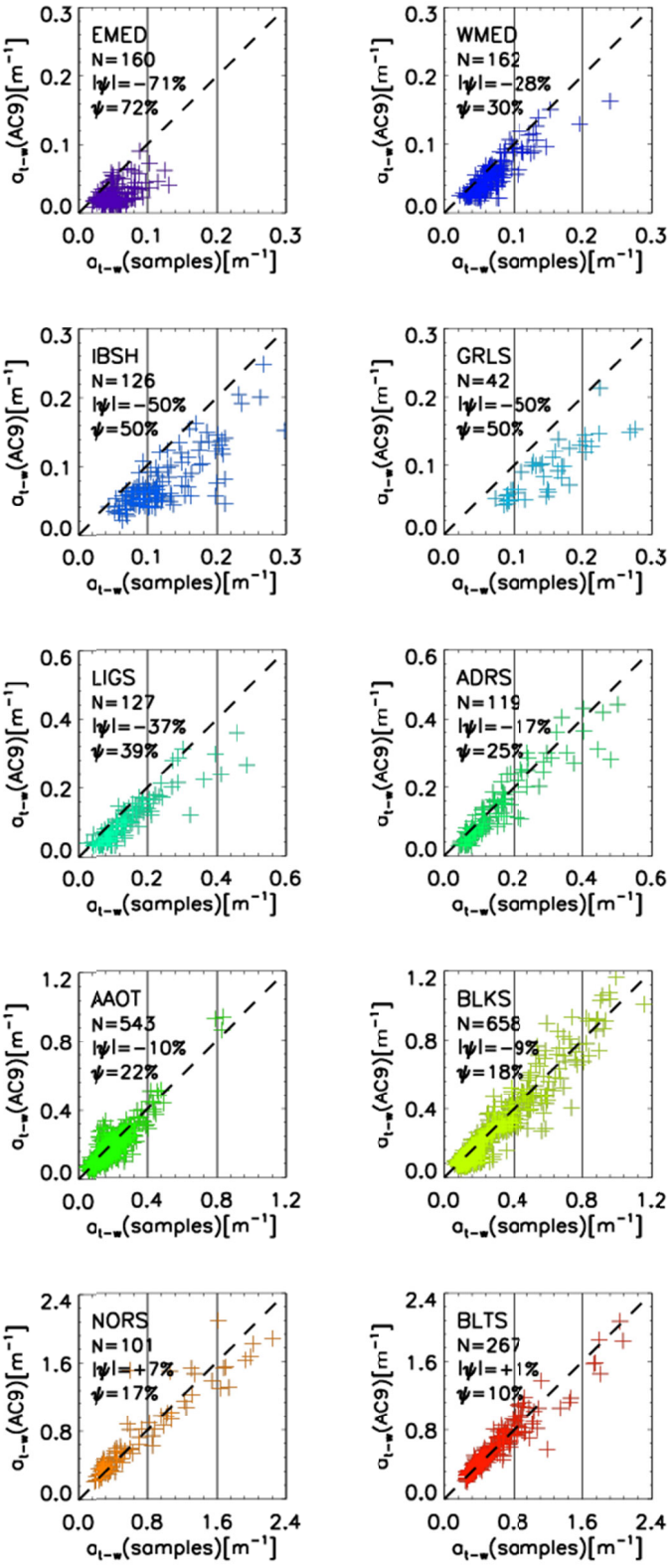
EMED
N=160
|ψ|=−71%
ψ=72%
WMED
N=162
|ψ|=−28%
ψ=30%
IBSH
N=126
|ψ|=−50%
ψ=50%
GRLS
N=42
|ψ|=−50%
ψ=50%
LIGS
N=127
|ψ|=−37%
ψ=39%
ADRS
N=119
|ψ|=−17%
ψ=25%
AAOT
N=543
|ψ|=−10%
ψ=22%
BLKS
N=658
|ψ|=−9%
ψ=18%
NORS
N=101
|ψ|=+7%
ψ=17%
BLTS
N=267
|ψ|=+1%
ψ=10%
a_t−w(AC9)[m^−1]
a_t−w(samples)[m^−1]

676
677

Figure 5. Scatter plot of AC9 derived $a_{t\text{-}w}$(AC9) and laboratory measurements performed on water samples $a_{t\text{-}w}$(samples), of the water absorption coefficient (water excluded) determined at the 443 nm center-wavelength for the diverse CoASTS and BioMaP marine regions. N indicates the number of samples while $|\psi|$ and ψ indicate the mean of absolute (unsigned) percent differences and the mean of (signed) percent differences, respectively.

Table 5. Spectral values of $Q_n(\lambda)$ in units of sr at the 412, 443, 490, 510, 555 and 670 nm center-wavelengths for the CoASTS and BioMaP marine regions, determined from in-water radiometric profiles performed with cloud cover $C_C \leq 1/4$.

Region	412	443	490	510	555	670
EMED (N=127)	3.89±0.33	3.90±0.36	3.88±0.42	3.87±0.45	3.84±0.54	4.90±1.12
WMED (N=100)	4.08±0.36	4.14±0.41	4.20±0.46	4.21±0.48	4.19±0.52	4.96±0.76
IBSH (N=87)	4.18±0.37	4.22±0.38	4.26±0.43	4.26±0.45	4.24±0.51	4.58±0.59
GRLS (N=11)	3.97±0.33	4.08±0.37	4.14±0.38	4.12±0.37	4.00±0.34	4.18±0.38
LIGS (N=53)	4.52±0.40	4.54±0.36	4.57±0.36	4.59±0.38	4.66±0.44	5.14±0.58
ADRS (N=71)	4.47±0.65	4.39±0.57	4.33±0.54	4.34±0.55	4.40±0.62	4.98±0.95
AAOT (N=372)	4.56±0.56	4.43±0.51	4.33±0.49	4.33±0.50	4.41±0.58	5.02±0.84
BLKS (N=401)	4.51±0.54	4.49±0.57	4.47±0.59	4.47±0.59	4.47±0.59	5.06±0.80
NORS (N=27)	4.70±0.60	4.71±0.57	4.69±0.54	4.67±0.53	4.60±0.50	4.90±0.48
BLTS (N=87)	4.93±0.69	5.09±0.74	5.18±0.78	5.16±0.76	4.99±0.66	5.20±0.86

Figure 6 shows trilinear (ternary) plots of the absorption coefficients $a_{ys}(443)$, $a_{dt}(443)$ and $a_{ph}(443)$, expressed in percent of the total absorption (*i.e.*, with respect to $a_{ys}(443)+a_{dt}(443)+a_{ph}(443)$), displayed with values increasing in the counter-clockwise direction (Harris 1999). These results exhibit very few cases characterized by dominance of absorption by particles with a_{ph} and a_{dt} values close to the upper and lower right apexes, respectively. Conversely, most of the cases indicate dominance of absorption by coloured dissolved organic matter: see the a_{ys} values near the lower left apex). This is particularly evident for the oligotrophic waters of the Eastern Mediterranean Sea (EMED), and by the patterns characterizing the oligotrophic-mesotrophic waters of the Western Mediterranean Sea (WMED), the optically complex water of the Black Sea (BLKS) and the highly absorbing waters of the Baltic Sea (BLTS).

The specific results shown for the Mediterranean Sea (*i.e.*, EMED and WMED), which may suggest inconsistency with the definition of Case-1 waters (IOCCG 2000), are supported by an independent study from Pérez et al. (2016).

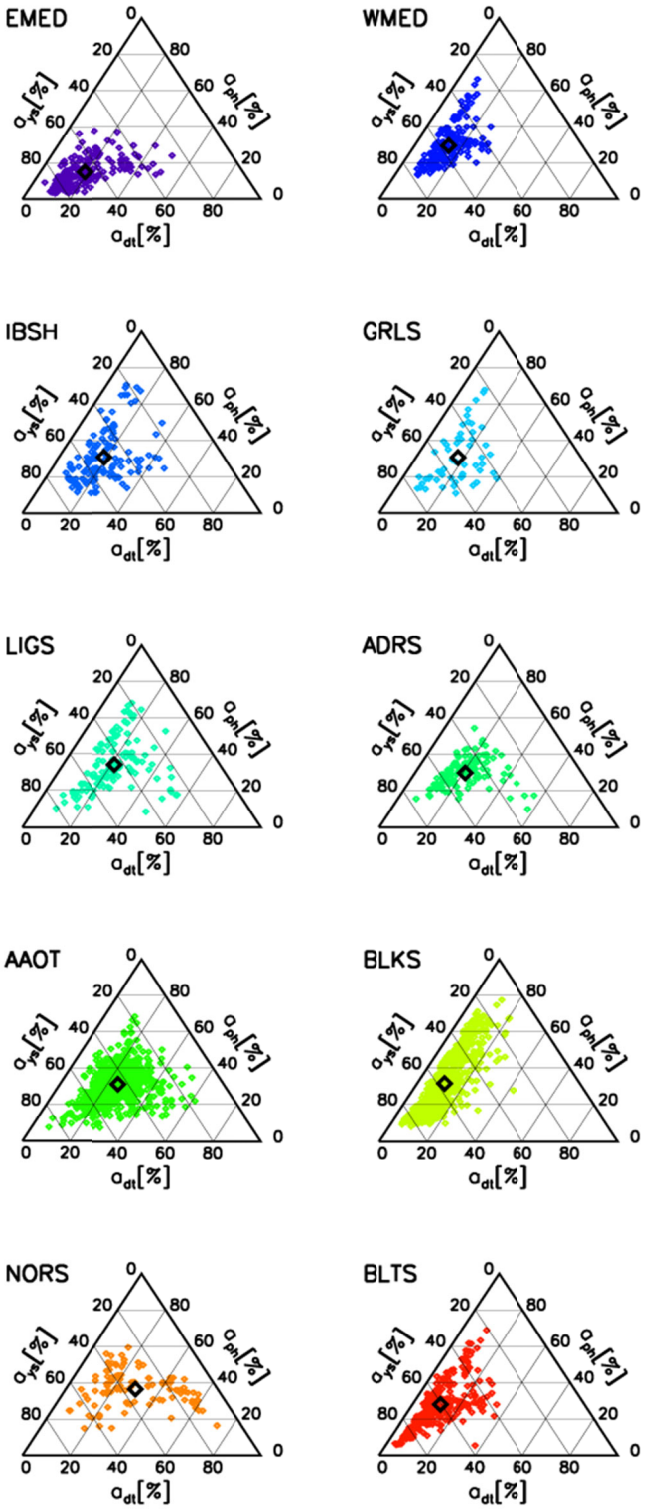

Figure 6. Trilinear (ternary) plots of the absorption coefficients a_{ys}, a_{dt} and a_{ph} expressed in percent of the total absorption (*i.e.*, with respect to $a_{ys}+a_{dt}+a_{ph}$) at the 443 nm center-wavelength. The empty black square indicates the mean of the plotted values.

Parameters determined from the exponential fit versus wavelength of $a_{dt}(\lambda)$ and $a_{ys}(\lambda)$, and the power law fit of $b_b(\lambda)$ versus wavelength, are provided in Tables 6-8. Specifically, the spectral values of $a_{dt}(\lambda)$ and $a_{ys}(\lambda)$ were fitted within the 412-665 nm spectral interval using

$$a_{dt}(\lambda) = A_{dt} \exp(-S_{dt}(\lambda - 412)) + B_{dt} \quad (8)$$

and

$$a_{ys}(\lambda) = A_{ys} \exp(-S_{ys}(\lambda - 412)) + B_{ys}, \quad (9)$$

where A_{dt} and A_{ys} indicate the absorption coefficients fitted at 412 nm, S_{dt} and S_{ys} the slope of the exponential function, and, B_{dt} and B_{ys} account for the background.

Conversely, the spectral values of $b_b(\lambda)$ at the center-wavelengths λ=442, 488, 510, 550 and 620 nm (excluding 676 or 671 nm due to potential perturbations by fluorescence), were fitted using

$$b_b(\lambda) = A_b\ (\lambda/442)^{-S_b}, \quad (10)$$

where A_b indicates the backscattering coefficient at 442 nm and S_b the slope of the power law function.

Table 6 shows mean values of the slope S_{dt} varying from 0.009 nm^{-1} for the Eastern Mediterranean Sea (EMED) up to 0.013 for the North Sea (NORS). Values of the bias B_{dt} naturally increase with A_{dt}: the largest value of B_{dt}= 0.067 m^{-1} is observed for the North Sea (NORS) that also exhibits the highest value of A_{dt}= 0.288 m^{-1}. Residuals R_{dt}, which also increase with A_{dt}, are quite minor suggesting a general good performance of the exponential fitting function.

Table 7 shows mean values S_{ys} varying from 0.012 nm^{-1} for the Eastern Mediterranean Sea (EMED) up to 0.019 nm^{-1} for the Baltic Sea (BLTS). The systematic negative biases B_{ys} across all marine regions are likely explained by the choice of zeroing the original spectra of absorption coefficients using values averaged in the 670-680 nm spectral interval. High residuals B_{ys} of 0.029 m^{-1} are observed for the Baltic Sea (BLTS). This is explained by a decreased performance of Eq. 9 when fitting spectra of absorption coefficients exhibiting values approaching or exceeding 1 m^{-1} at 412 nm. Still, all residuals B_{ys} expressed in percent of A_{ys} vary between 0.3 and 0.5%, except for the East Mediterranean Sea (EMED) showing a value of 0.9%.

As expected, also the values of S_b largely vary across the CoASTS and BiOMaP marine regions: in particular they exhibit values of 2.97 μm^{-1} for the East Mediterranean Sea (EMED), 2.06 μm^{-1} for the Iberian Shelf (IBSH) and 0.74 μm^{-1} for the North Sea (NORS). This is likely explained by an increase of the average particles size when going from the oligotrophic East Mediterranean Sea to the eutrophic and more sediment loaded North Sea.

Figure 7 and 8 shows the distribution of *Chla* and *SPM* across the CoASTS and BiOMaP marine regions. The very low concentrations characterizing the oligotrophic waters of the Eastern Mediterranean Sea (EMED) exhibiting mean *Chla* values of 0.09 $\mu g\ l^{-1}$ and mean *SPM* values of 0.27 mg l^{-1}, are remarkable. Conversely, *Chla* exhibits mean values in the range of 4-5 $\mu g\ l^{-1}$ for both the North Sea (NORS) and Baltic Sea (BLKS), while for the same marine regions *SPM* shows mean values of 9.96 and 1.53 mg l^{-1}, respectively. A log-normal distribution of both *Chla* and *SPM* is generally confirmed for the CoASTS and BiOMaP data.

753 Figure 9 displays the scatter plots of $b_{bp}(488)/b_p(488)$ versus *Chla*, where $b_p(488)$ is
754 determined by the difference between $c_{t\text{-}w}(488)$ and $a_{t\text{-}w}(488)$, while $b_{bp}(488)$ is determined from
755 $b_b(488)$ by subtracting the scattering coefficient of water $b_w(488)$ from Morel (1974). Results are
756 consistent with those shown by Twardowki et al. (2001) for a variety of experimental data, with
757 $b_{bp}(488)/b_p(488)$ typically varying between 0.003 and 0.025. Exception are some very low
758 values of $b_{bp}(488)/b_p(488)$ for EMED data likely explained by large measurement uncertainties.
759 Coherent with published results is also the generally higher value and higher scatter of
760 $b_{bp}(488)/b_p(488)$ in correspondence of low *Chla* concentrations.
761
762
763 Table 6. Parameters A_{dt}, S_{dt} and B_{dt} of the exponential fitting function (see Eq. 8) applied to the
764 values of $a_{dt}(\lambda)$. The quantity R_{dt} indicates the spectral average of absolute differences (*i.e.,*
765 residuals) between actual and fitted values.
766

Region	A_{dt} [m^{-1}]	S_{dt} [nm^{-1}]	B_{dt} [m^{-1}]	R_{dt} [m^{-1}]
EMED (N=190)	0.010±0.007	0.009±0.002	0.002±0.001	0.0000
WMED (N=186)	0.009±0.004	0.012±0.001	0.003±0.001	0.0000
IBSH (N=129)	0.024±0.022	0.011±0.001	0.006±0.005	0.0001
GRLS (N=54)	0.024±0.014	0.012±0.002	0.007±0.004	0.0000
LIGS (N=126)	0.032±0.026	0.011±0.002	0.007±0.004	0.0001
ADRS (N=120)	0.042±0.057	0.012±0.001	0.009±0.011	0.0000
AAOT (N=614)	0.048±0.031	0.012±0.001	0.009±0.005	0.0000
BLKS (N=692)	0.034±0.057	0.011±0.002	0.005±0.008	0.0001
NORS (N=102)	0.288±0.377	0.013±0.001	0.067±0.094	0.0005
BLTS (N=274)	0.095±0.125	0.011±0.002	0.011±0.017	0.0003

767
768
769 Table 7. Parameters A_{ys}, S_{ys} and B_{ys} of the exponential fitting function (see Eq. 9) applied to the
770 values of $a_{ys}(\lambda)$. The quantity R_{ys} indicates the spectral average of absolute differences (*i.e.,*
771 residuals) between actual and fitted values.
772

Region	A_{ys} [m^{-1}]	S_{ys} [nm^{-1}]	B_{ys} [m^{-1}]	R_{ys} [m^{-1}]
EMED (N=182)	0.056±0.025	0.012±0.004	-0.005±0.007	0.0004
WMED (N=183)	0.059±0.019	0.013±0.003	-0.002±0.002	0.0002
IBSH (N=129)	0.093±0.036	0.014±0.003	-0.004±0.005	0.0004
GRLS (N=54)	0.107±0.027	0.014±0.003	-0.004±0.003	0.0003
LIGS (N=126)	0.091±0.052	0.014±0.004	-0.004±0.004	0.0004
ADRS (N=120)	0.114±0.058	0.016±0.002	-0.002±0.002	0.0003
AAOT (N=592)	0.132±0.059	0.017±0.004	-0.003±0.005	0.0003
BLKS (N=693)	0.205±0.122	0.017±0.002	-0.004±0.003	0.0005
NORS (N=102)	0.280±0.094	0.017±0.002	-0.004±0.002	0.0007
BLTS (N=274)	0.606±0.330	0.019±0.001	-0.004±0.003	0.0029

773
774

775 Table 8. Parameters A_b and S_b of the power low fitting function (see Eq. 10) applied to the values
776 of $b_b(\lambda)$ at λ= 443, 488, 510, 555 and 620 nm for the CoASTS and BioMaP marine regions. The
777 quantity R_b indicates the spectral average of absolute differences (*i.e.,* residuals) between actual
778 and fitted data.

Region	A_b [m^{-1}]	S_b [μm^{-1}]	R_b [m^{-1}]
EMED (N=184)	0.0034±0.0008	2.97±0.56	0.0001
WMED (N=186)	0.0041±0.0009	2.54±0.42	0.0001
IBSH (N=127)	0.0051±0.0025	2.06±0.55	0.0002
GRLS (N=52)	0.0048±0.0024	2.25±0.33	0.0001
LIGS (N=126)	0.0091±0.0072	1.83±0.64	0.0002
ADRS (N=111)	0.0103±0.0071	1.74±0.57	0.0002
AAOT (N=479)	0.0136±0.0078	1.35±0.42	0.0004
BLKS (N=534)	0.0126±0.0077	1.99±0.53	0.0006
NORS (N=57)	0.0207±0.0157	0.74±0.38	0.0005
BLTS (N=256)	0.0118±0.0082	1.15±0.49	0.0003

779
780

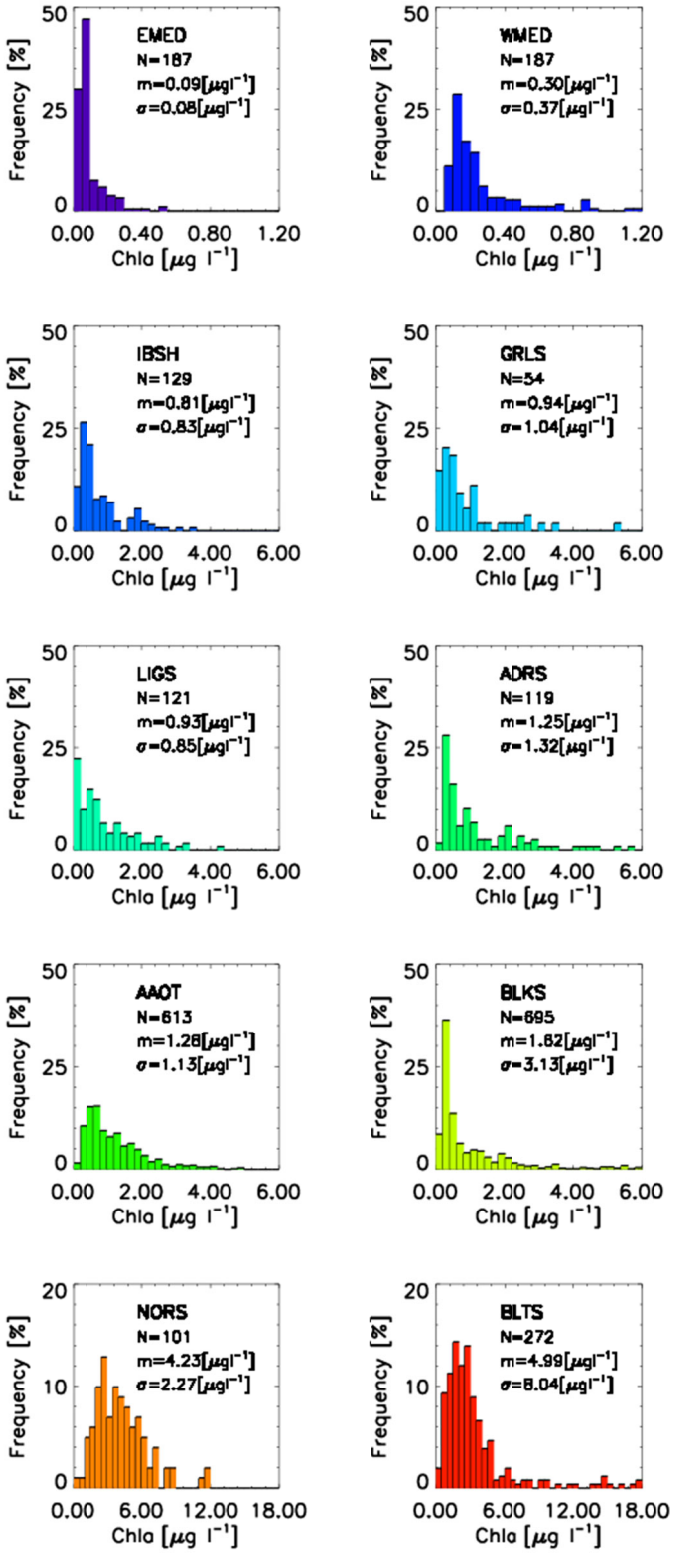

781
782 Figure 7. Frequency distribution of *Chla* across the CoASTS and BioMaP marine regions. N
783 indicates the number of stations, *m* the mean values and σ the standard deviation.

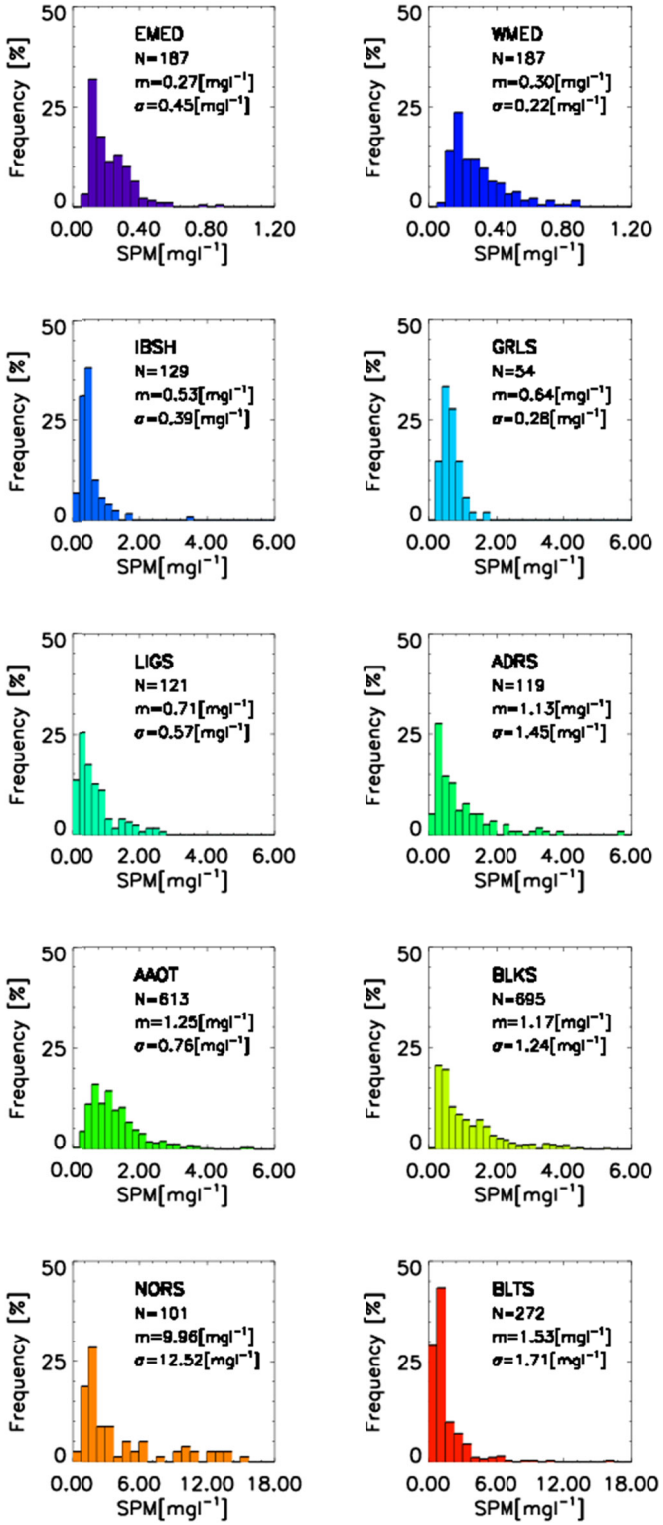

Figure 8. Frequency distribution of *SPM* across the CoASTS and BioMaP marine regions. N indicates the number of stations, *m* the mean values and σ the standard deviation.

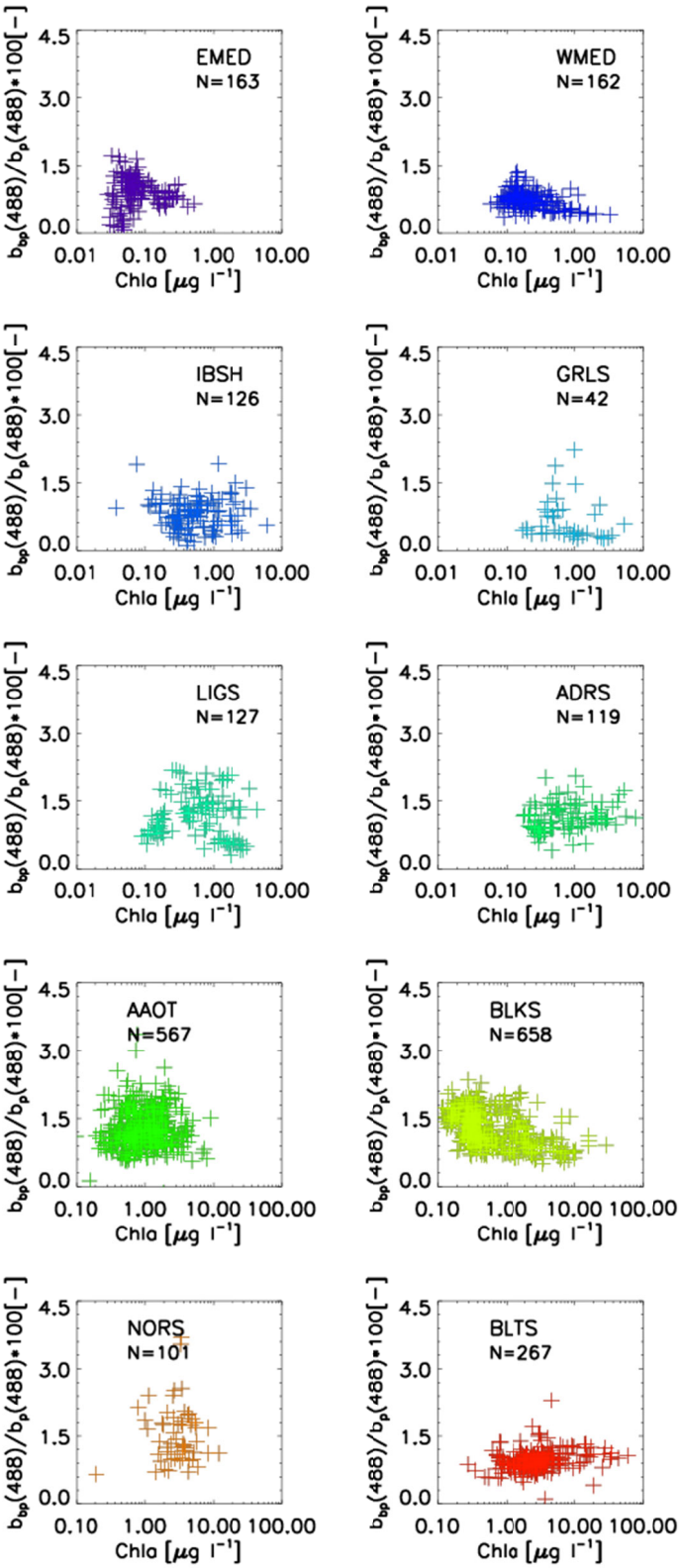

Figure 9. Scatter plot $b_{bp}(488)/b_p(488)$ and *Chla* for the diverse CoASTS and BioMaP marine regions. N indicates the number of samples.

Table 9. Mean values of the *Chla* specific absorption coefficient a_{ph}* at 443 nm.

Region	a_{ph}*(443) [m^2mg^{-1}]
EMED (N=210)	0.090±0.029
WMED (N=190)	0.083±0.018
IBSH (N=129)	0.062±0.050
GRLS (N=54)	0.063±0.018
LIGS (N=121)	0.065±0.021
ADRS (N=119)	0.053±0.034
AAOT (N=613)	0.052±0.022
BLKS (N=695)	0.084±0.046
NORS (N=101)	0.061±0.108
BLTS (N=272)	0.047±0.014

Table 9 provides the mean specific absorption coefficients $a_{ph}^*(443)$ determined by the ratio of $a_{ph}(443)$/*Chla* across the various CoASTS and BioMaP marine regions. These mean values of $a_{ph}^*(443)$ vary from 0.047 m^2mg^{-1} in the Baltic Sea (BLT) to 0.090 m^2mg^{-1} in the Eastern Mediterranean Sea. It is warned that these latter values could be challenged by increased relative uncertainties in the determination of both $a_{ph}(443)$ and *Chla*.

6. Summary and conclusions

The CoASTS and BiOMaP measurement programs led by the JRC Marine Optical Laboratory benefitting of the collaboration of a number of European institutions and various funding programs, were conceived to support satellite ocean color applications. Between 1995 and 2022 the two programs produced time-series at the AAOT site in the northern Adriatic Sea and geographically distributed bio-optical measurements across the major European Seas. The measurements delivered by the two programs beyond December 1998 include identical quantities and are characterized by standardization of measurement methods, instruments, data processing and quality assurance/control schemes.

This work introduced the CoASTS-BiOMaP data set comprising the near surface data products from the CoASTS and BiOMaP measurement programs of major relevance for satellite ocean color validation activities and bio-optical modelling.

7. Author contributions

Both authors, Giuseppe Zibordi and Jean-François Berthon, who implemented and co-led the CoASTS and BiOMaP programs, contributed to the generation of the data set and to the writing of the manuscript. Giuseppe Zibordi was a JRC Scientific Officer since the conception and up to the end of the CoASTS and BiOMaP programs.

8. Competing interests

Both authors declare no competing interest.

9. Data availability

Interested researchers can download the CoASTS-BiOMaP data set at https://doi.pangaea.de/10.1594/PANGAEA.971945 (Zibordi and Berthon, 2024). The original field measurements leading to the creation of this data set are currently not publicly available. However, they can be obtained from the authors upon a reasonable request.

10. Acknowledgments

The technical contributions to field measurements and laboratory analysis of many JRC and international colleagues are fully acknowledged: Cristina Targa, Stefania Grossi, Dirk Van der Linde, Lukasz Jankowski, Lyudmila Kamburska, Davide D'Alimonte, Marco Talone, Pietro Sciuto, Ilaria Cazzaniga, Jean Verdebout, Elisabetta Canuti, Alessandro Marchetti, Violeta Slabakova, Natalia Slabakova, Carolina Sa', Simone Colella, Gianluca Volpe, Seppo Kaitala, Jukka Seppala, Aleksandra Mazur.

Finally, Jaime Pitarch and Mike Twardowski are acknowledged for their comments to the submitted manuscript.

11. Funding support

Direct or indirect (through ship time) support to CoASTS and BiOMaP activities was provided by: the JRC through the EOSS and COLORS institutional projects, the European Union through the MAST-III, EUROFLEETS and JERICO programs, the North Atlantic Treaty Organization (NATO) through the Science for Peace Program, the US National Aeronautics and Space Administration (NASA), the European Space Agency (ESA), the Romanian Space Agency (ROSA), the Institute of Oceanology of the Bulgarian Academy of Sciences, the Institute of Oceanology of the Polish Academy of Sciences, the Finnish Environment Institute, the Italian National Research Council, the Portuguese Hydrographic Institute, the Italian Hydrographic Institute, the Royal Belgian Institute of Natural Sciences, the Hellenic Centre for Marine Research, the Université du Littoral Côte d' Opale.

The contribution of Giuseppe Zibordi to the finalization of this work was supported by the National Aeronautics and Space Administration through the GESTAR-II program under award number 80NSSC22M0001, while the contribution of Jean-François Berthon was supported by DG DEFIS (the European Commission Directorate-General for Defence Industry and Space) and the Copernicus Programme.

12. References

Belward, A., J. Hartstra, B. Baruth, P. Beck, C. Carmona Moreno, P. Churchill, M. Craglia, R. Crandon, D. Ehrlich, H. Eva, J. Fortuny Guasch, K.T. K.T., T. Kemper, H. Kerdiles, H., O. Leo, P. Loudjani, G. Maenhout, P. Milenov, M. Pesaresi, B. Pinty, G. Zibordi, and J. Kreysa, 2022: A history of remote sensing at the JRC, Publications Office of the European Union, Luxembourg, ISBN 978-92-76-49465-2, JRC127849.

Berthon, J. F., F. Mélin, and G. Zibordi, 2008: Ocean colour remote sensing of the optically complex European seas. In *Remote sensing of the European seas* (pp. 35–52). Springer, Dordrecht.

Berthon, J-F., G. Zibordi, J.P. Doyle, S. Grossi, D. van der Linde, and C. Targa, 2002: Coastal Atmosphere and Sea Time Series (CoASTS), Part 2: Data Analysis. *NASA Tech. Memo.*

2002–206892, Vol. 20, S.B. Hooker and E.R. Firestone, Eds., NASA Goddard Space Flight Center, Greenbelt, Maryland, 25 pp.

Boss, E., W. H. Slade, M. Behrenfeld, and G. Dall'Olmo, 2009: Acceptance angle effects on the beam attenuation in the ocean. *Opt. Express*, **17**(3), 1535–1550.

D'Alimonte, D., E.B. Shybanov, G. Zibordi, and T. Kajiyama, 2013: Regression of in-water radiometric profile data. *Opt. Express*, **21**(23), 27707–27733.

Doyle, J. P., and G. Zibordi, 2002: Optical propagation within a three-dimensional shadowed atmosphere–ocean field: application to large deployment structures. *Appl. Opt.*, **41**(21), 4283–4306.

Doyle, J.P., S.B. Hooker, G. Zibordi, and D. van der Linde, 2003: Validation of an In-Water, Tower-Shading Correction Scheme. NASA Tech. Memo. 2003–206892, Vol. 25, S.B. Hooker and E.R. Firestone, Eds., NASA Goddard Space Flight Center, Greenbelt, Maryland, 32 pp.

Doxaran D., E. Leymarie, B. Nechad, A. Dogliotti, K. Ruddick, P. Gernez, and E. Knaeps, 2016: Improved correction methods for field measurements of particulate light backscattering in turbid waters. *Opt. Express* **24**, 3615–3637.

Ferrari, G. M., M. D. Dowell, S. Grossi, and C. Targa, 1996: Relationship between the optical properties of chromophoric dissolved organic matter and total concentration of dissolved organic carbon in the southern Baltic Sea region. *Mar. Chem.*, **55**(3–4), 299–316.

Ferrari, G. M., and S. Tassan, 1999: A method using chemical oxidation to remove light absorption by phytoplankton pigments. *J. Phycology*, **35**(5), 1090–1098.

Gergely, M., and G. Zibordi, 2013: Assessment of AERONET-OC Lwn uncertainties. *Metrologia*, **51**(1), 40.

Harris, R. L., 1999: *Information graphics: A comprehensive illustrated reference*. Oxford University Press, USA, 448 pp.

Hooker S. B., C. S. Thomas, L. Van Heukelem, M. E. Russ, J. Ras, H. Claustre, L. Clementson, E. Canuti, J.-F. Berthon, J. Perl, and C. Normandeau, 2010: The fourth SeaWiFS HPLC analysis round-Robin experiment (SeaHARRE–4). NASA. Technical Memorandum −2010–215857. NASA Goddard Space Flight Center, Greenbelt, Maryland, 75 pp.

IOCCG, 2000: Remote Sensing of Ocean Colour in Coastal, and Other Optically-Complex, Waters. Sathyendranath, S. (ed.), *Reports of the International Ocean-Colour Coordinating Group*, No. 3, IOCCG, Dartmouth, Canada

IOCCG, 2019: IOCCG Ocean optics and biogeochemistry protocols for satellite ocean colour sensor validation: In situ optical radiometry. *IOCCG Protocols Series*, Volume n. 3, IOCCG, Dartmouth, Canada (https://ioccg.org/wp-content/uploads/2019/12/protocols-insitu-optical-radiometry-v3.0.pdf).

IOCCG (2019). IOCCG Ocean optics and biogeochemistry protocols for satellite ocean colour sensor validation: Measurement protocol of absorption by chromophoric dissolved organic matter (CDOM) and other dissolved materials *Volume n. 5.0, IOCCG, Dartmouth, Canada* (https://ioccg.org/wp-content/uploads/2019/10/cdom_abs_protocol_public_draft-19oct-2019-sm.pdf *).*

Jeffrey, S.W., R.F.C. Mantoura, and S.W. Wright (Eds.), 1997: *Phytoplankton Pigments in Oceanography: Guidelines to Modern Methods.* UNESCO Publishing, Paris, 661 pp.

Maffione, R. A., and D. R. Dana, 1997: Instruments and methods for measuring the backward-scattering coefficient of ocean waters. *Appl. Opt.*, **36**(24), 6057–6067.

Morel, A., 1974: Optical properties of pure water and pure seawater. *Optical Aspects of Oceanography*.

915 Morel, A., and Y.-H. Ahn, 1990: Optical efficiency factors of free-living marine bacteria:
916 Influence of bacterioplankton upon the optical properties and particulate organic carbon in
917 oceanic waters, *J. Mar. Res.,* **48,** 145–175.
918 Morel, A., D. Antoine, and B. Gentili, 2002: Bidirectional reflectance of oceanic waters:
919 accounting for Raman emission and varying particle scattering phase function. *Appl.*
920 *Opt.*, **41**(30), 6289–6306.
921 Mueller, J. L., and R. W. Austin, 1995: Ocean Optics Protocols for Sea-WiFS Validation,
922 Revision 1. *NASA Tech. Memo. 104566, Vol. 25,* S.B. Hooker and E.R. Firestone, Eds.,
923 NASA Goddard Space Flight Center, Greenbelt, Maryland, 67 pp.
924 Pérez, G. L., M. Galí, S. J. Royer, H. Sarmento, J. M. Gasol, C. Marrasé, and R. Simó, 2016:
925 Bio-optical characterization of offshore NW Mediterranean waters: CDOM contribution to
926 the absorption budget and diffuse attenuation of downwelling irradiance. *Deep Sea Res. Part I*
927 *Oceanogr.*, **114**, 111–127.
928 Smith, R. C., and K. S. Baker, 1981: Optical properties of the clearest natural waters (200–800
929 nm). *Appl. Opt.*, **20**(2), 177–184.
930 Stockley, N. D., R. Röttgers, D. McKee, I. Lefering, J. M. Sullivan, and M. S. Twardowski,
931 2017: Assessing uncertainties in scattering correction algorithms for reflective tube absorption
932 measurements made with a WET Labs AC-9. *Opt. Express*, **25**(24), A1139–A1153.
933 Stramski, D., and D. A. Kiefer, 1991: Light scattering by microorganisms in the open
934 ocean. *Progr. Oceanogr.*, **28**(4), 343–383.
935 Strickland, J.D.H., and T.R. Parsons, 1972: A practical handbook of sea water analysis. *Fish.*
936 *Res. Board. Canada,* 310 pp.
937 Tassan, S., and G. M. Ferrari, 1995: An alternative approach to absorption measurements of
938 aquatic particles retained on filters. *Limnol. Oceanogr.*, **40**(8), 1358–1368.
939 Tassan, S., G. M. Ferrari, A. Bricaud, and M. Babin, 2000: Variability of the amplification factor
940 of light absorption by filter-retained aquatic particles in the coastal environment. *J. Plankton*
941 *Res.*, **22**(4), 659–668.
942 Thuillier, G., M. Hersé, T. Foujols, W. Peetermans, D. Gillotay, P. C. Simon, and H. Mandel,
943 2003: The solar spectral irradiance from 200 to 2400 nm as measured by the SOLSPEC
944 spectrometer from the ATLAS and EURECA missions. *Sol. Phys.*, **214**(1), 1–22.
945 Twardowski, M. S., H. Claustre, S. A. Freeman, D. Stramski, and Y. Huot, 2007: Optical
946 backscattering properties of the" clearest" natural waters. *Biogeosciences*, **4(**6), 1041–1058.
947 Twardowski, M. S., E. Boss, J. B. Macdonald, W. S. Pegau, A. H. Barnard, and J. R. V.
948 Zaneveld, 2001: A model for estimating bulk refractive index from the optical backscattering
949 ratio and the implications for understanding particle composition in case I and case II
950 waters. *J. Geophys. Res. Oceans*, **106**(C7), 14129–14142.Valente, A. and coauthors, 2016: A
951 compilation of global bio-optical in situ data for ocean-colour satellite applications. *Earth*
952 *Syst. Sci. Data*, **8**(1), 235–252.
953 Van der Linde, D., 1998: Protocol for total suspended matter estimate. *JRC Technical Note I-98-*
954 *182*, Joint Research Centre of the European Commission, Ispra, Italy, 15 pp.
955 Van Heukelem, L., and C. S. Thomas, 2001: Computer-assisted high-performance liquid
956 chromatography method development with applications to the isolation and analysis of
957 phytoplankton pigments. *J. Chromatogr. A*, **910**(1), 31–49.
958 Voss, K. J., and S. Flora, 2017: Spectral dependence of the seawater–air radiance transmission
959 coefficient. *J. Atmos. Ocean. Technology*, **34**(6), 1203–1205.

Werdell, P. J., and S. W. Bailey, 2005: An improved in-situ bio-optical data set for ocean color algorithm development and satellite data product validation. *Remote Sens. Environ.*, **98**(1), 122–140.

Wet Labs, 2006: AC meter Protocol. WET Labs, Inc. Philomath, Oregon, 75 pp. https://misclab.umeoce.maine.edu/ftp/classes/OO2015/Instruments/ac9acs/acprotocol.pdf .

Whitmire, A. L., E. Boss, T. J. Cowles, and W. S. Pegau, 2007: Spectral variability of the particulate backscattering ratio. *Opt. Express*, **15**(11), 7019–7031.

World Meteorological Organization, 1983: *Guide to the Meteorological Instruments and Methods of Observation,* WMO–N.8, 517 pp.

Zaneveld, J. R. V., J. C. Kitchen, A. Bricaud, and C. C. Moore, 1992: Analysis of in-situ spectral absorption meter data. In *Ocean Optics XI* Proc. Soc. Photo-Optical Instrum. Eng. (SPIE), 1750, 187 200.

Zhang, X., D. Stramski, R. A. Reynolds, and E. R. Blocker, 2019: Light scattering by pure water and seawater: the depolarization ratio and its variation with salinity. *Appl. Opt.*, **58**(4), 991–1004.

Zhang, X., L. Hu, and M. X. He, 2009: Scattering by pure seawater: Effect of salinity. *Opt. Express*, **17**(7), 5698–5710.Zibordi, G., 2006: Immersion factor of in-water radiance sensors: assessment for a class of radiometers. *J. Atmos. Ocean. Technology*, **23**(2), 302–313.

Zibordi, G., and J.-F. Berthon, 2024: Coastal Atmosphere & Sea Time Series (CoASTS) and the Bio-Optical mapping of Marine optical Properties (BiOMaP): the near-surface marine bio-optical data set. Accessible at: https://doi. pangaea.de/10.1594/PANGAEA.968716.

Zibordi, G., J.-F. Berthon, J.P. Doyle, S. Grossi, D. van der Linde, C. Targa, and L. Alberotanza, 2002: Coastal Atmosphere and Sea Time Series (CoASTS), Part 1: A Tower-Based Long-Term Measurement Program. *NASA Tech. Memo. 2002–206892, Vol. 19,* S.B. Hooker and E.R. Firestone, Eds., NASA Goddard Space Flight Center, Greenbelt, Maryland, 29 pp.

Zibordi, G., J.-F. Berthon, F. Mélin, and D. D'Alimonte, 2011: Cross-site consistent in situ measurements for satellite ocean color applications: The BiOMaP radiometric dataset. *Remote Sens. Environ.*, **115**(8), 2104–2115.

Zibordi, G., and B. Bulgarelli, 2007: Effects of cosine error in irradiance measurements from field ocean color radiometers. *Appl. Opt.*, **46**(22), 5529–5538.

Zibordi, G., J. P. Doyle, and S. B. Hooker, 1999: Offshore tower shading effects on in-water optical measurements. *J. Atmos. Ocean. Technology*, **16**(11), 1767–1779.

Zibordi, G., B. N. Holben, M. Talone, D. D'Alimonte, I. Slutsker, D. M. Giles, and M. G. Sorokin, 2021: Advances in the ocean color component of the aerosol robotic network (AERONET-OC). *J. Atmos. Ocean. Technology*, **38**(4), 725–746.

Zibordi, G., S. B. Hooker, J. Mueller, and G. Lazin, 2004: Characterization of the immersion factor for a series of in-water optical radiometers. *J. Atmos. Ocean. Technology*, **21**(3), 501–514.

Zibordi, G., and K. J. Voss, 2010: Field radiometry and ocean color remote sensing. In *Oceanography from Space* (pp. 307–334). Springer, Dordrecht.

Appendix A: Acronyms

AAOT	Acqua Alta Oceanographic Tower
ADRS	Adriatic Sea
AERONET-OC	Ocean Color component of the Aerosol Robotic Network
BiOMaP	Bio-Optical mapping of Marine Properties
BLKS	Black Sea
BLTS	Baltic Sea
CDOM	Colored Dissolved Organic Matter
CoASTS	Coastal-Atmosphere and Sea Time-Series
CTD	Conductivity, temperature and depth
EMED	Eastern Mediterranean Sea
GRLS	Greenland Sea
HPLC	High-Pressure Liquid Chromatography
IBS	Iberian Shelf
LIGS	Ligurian Sea
JRC	Joint Research Center
NASA	National Aeronautics and Space Administration
NIST	National Institute of Standards and Technology
NORS	North Sea
NPL	National Physical Laboratory
SeaWiFS	Sea-viewing Wide Field-of-view Sensor
WMED	Western Mediterranean Sea
WiSPER	Wire-Stabilized Profiling Environmental Radiometer